Check for updates

Liquid-phase electron microscopy imaging of cellular and biomolecular systems

John W. Smith[a] and Qian Chen [ID] *[abcd]

The ongoing development of liquid-phase electron microscopy methods—in which specimens are kept fully solvated in the microscope by encapsulation in transparent, vacuum-tight chambers—is making it possible to investigate a wide variety of nanoscopic dynamic phenomena at the single-particle level, and with nanometer to atomic resolution. As such, there has been growing motivation to make liquid-phase electron microscopy tools applicable not only to inorganic materials, like metals, semiconductors, and ceramics, but also to "soft" materials such as biomolecules and cells, whose nanoscale dynamics and organization are intricately tied to their functionality. Here we review efforts toward making this an experimental reality, summarizing recent liquid-phase electron microscopy studies of whole cells, assembling peptides, and even individual proteins. Successes and challenges are discussed, as well as strategies to maximize the amount of accessible information and minimize the impact of the electron beam. We conclude with an outlook on the potential of liquid-phase electron microscopy to provide new insight into the rich and functional dynamics occurring in biological systems at the microscopic to molecular level.
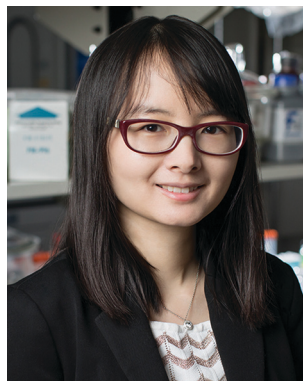
[a] Department of Materials Science and Engineering, University of Illinois at Urbana–Champaign, Urbana, IL 61801, USA. E-mail: qchen20@illinois.edu
[b] Department of Chemistry, University of Illinois at Urbana–Champaign, Urbana, IL 61801, USA
[c] Materials Research Laboratory, University of Illinois at Urbana–Champaign, Urbana, IL 61801, USA
[d] Beckman Institute for Advanced Science and Technology, University of Illinois at Urbana–Champaign, Urbana, IL 61801, USA
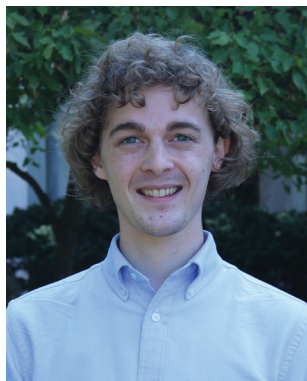
John W. Smith obtained his Bachelor's degree in Materials Science and Engineering at the University of Illinois at Urbana–Champaign in 2016. He is currently a PhD candidate there in Professor Qian Chen's group, and is interested in finding connections between soft matter physics and biology at the nanometer scale. In 2018 he received the 3M graduate student fellowship for his research work. Smith can be reached by email at jwsmith6@illinois.edu.

John W. Smith

Qian Chen is an assistant professor in the Department of Materials Science and Engineering at the University of Illinois at Urbana–Champaign since 2015. She received her PhD degree from the same department in 2012. Her research focuses on electron microscopy-based imaging, understanding, and engineering of soft materials, such as nanoparticle and colloidal self-assembly, protein transformation, battery materials, and energy-efficient filtration. Her awards include the American Chemistry Society's (ACS) Victor K. LaMer Award in 2015, the Air Force Office of Scientific Research Young Investigator Award in 2017, the National Science Foundation CAREER Award in 2018, a Sloan Fellowship in 2018, and the ACS Unilever Award (2018). She also was recognized on the Forbes 30 Under 30 Science List in 2016. Chen can be reached by email at qchen20@illinois.edu.

Qian Chen

1. Introduction

Life on Earth and liquid water are intertwined with each other across a tremendous range of scales, from years and kilometers to femtoseconds and angstroms. For example, not only is the water of Earth's surface home to the vast majority and greatest diversity of animal species,[1,2] it also provides food and resources for terrestrial life and, on periods from days to months, governs the world's tides, climate, and agriculture.[3,4] The human body, too, is about 70% water, which is necessary for phenomena ranging from thermal regulation and pH maintenance[5] to the exchange of nutrients and information across trillions of cells.[6,7] At this scale, comings and goings of water are linked to metabolism cycles in animals or flowering patterns in plants. It is at the microscopic and nano-scales, however, where cells divide, synapses fire, proteins fold, and enzymes catalyze, that the bond between life and liquid water is at its strongest and most complex. Life processes in this domain occur not just within, but using liquid water, and all its physical and chemical idiosyncrasies (its shape, hydrogen bonding capability, polarity, *etc.*) come into play to drive the formation and dynamics of biologically relevant structures.[8,9] As such, many decades of scientific research have been devoted to understanding the structure and dynamics of biological systems—cells, membranes, proteins, nucleic acids—in their native liquid environment at the microscopic to molecular level.

The experimental arsenal for structural and dynamic characterization of biological systems today contains a wide variety of tools. On the one hand, ensemble techniques such as nuclear magnetic resonance spectroscopy,[10–12] X-ray scattering and diffraction,[13,14] and a plethora of other spectroscopy methods (electron paramagnetic resonance, infrared spectroscopy, circular dichroism, *etc.*)[15–18] offer powerful ways to investigate the structure, fluctuations, or assembly of hydrated biomolecular systems on a global level. These techniques are widely used to study phenomena like protein folding,[19,20] determine the structure of proteins in large crystals,[13,21] and resolve atomic scale details of protein–protein interactions[22,23] in homogeneous environments, where ensemble-wide averaging is applicable. On the other hand, for many biological systems, "real-space" and imaging-based methods are more valuable, since they can accommodate the heterogeneous, independent, and not necessarily synchronized components characteristic of real living systems. Optical imaging techniques in particular, such as phase contrast microscopy,[24,25] confocal fluorescence microscopy,[26,27] and total internal reflection microscopy,[28] have helped reveal how cells are organized, how they divide, how transport occurs in the cellular milieu, and more, simply through direct, real-time observation. Nevertheless, fundamental physical constraints (namely, the diffraction limit of visible light) restrict optical imaging methods to a resolution of about 200 nm, which is far from the level needed to probe the many critical biological structures and phenomena which occur at the nanometer scale, accessible by the spectroscopy methods described above. While the family of "super-resolution" fluorescence imaging techniques, including stimulated emission depletion microscopy,[29,30] photoactivated localization microscopy,[31–33] stochastic optical reconstruction microscopy,[34] and variations thereof[35,36] can push this resolution limit to approximately 20 nm and locate individual molecules extremely precisely,[37,38] they cannot necessarily be used to observe the processes (notably, protein conformation or shape fluctuations, protein–protein interactions, *etc.*) occurring within these tiny regions. Moreover, fluorescent signals coming from features of interest must be sufficiently separated either in space (low spatial density) or time (through flickering, for instance) in order to be localized with such precision, the latter of which can adversely affect temporal resolution.

To overcome the physical resolution limits of optical microscopy, a natural alternative is to image using electrons. More specifically, because electrons have a wavelength orders of magnitude smaller than that of visible light, electron microscopy can achieve atomic resolution or better, both for inorganic samples[39,40] and, especially with the advent of cryogenic electron microscopy (cryo-EM) techniques, organic and biological materials.[41–43] However, a long-standing and fundamental limitation of conventional electron microscopy has been that it requires the use of a vacuum environment, void of liquid and vapor, for operation.[44] Usually, specimens must either be dried,[45,46] fixed in resin,[47,48] or flash-frozen in vitreous ice[42,43,46] to be examined in an electron microscope, all of which inherently quench the rich and, more importantly, functionally relevant dynamics characteristic of biological materials. While there were attempts in the early days of electron microscopy to overcome this limitation[44,49] using elaborate differential pumping schemes[44,50] or thin windows,[51] some even by Ernst Ruska himself (who would eventually win the first Nobel Prize for electron microscopy),[52] at the time these methods were not widely practicable, and cryo-EM became the predominant tool to investigate the structure of hydrated (albeit immobilized) biological materials in the electron microscope. Recently, cryo-EM-based strategies utilizing high-speed microfluidic spraying[53,54] or computational tools[55] have been devised to extract distinct conformational "snapshots" of molecules in vitreous ice, but these snapshots must then be assembled into a continuous dynamic pathway empirically, without direct knowledge of the time scales involved, and a major caveat is that not all states are necessarily captured in such experiments; flexible intermediates or sparsely populated configurations may be altogether lost.

In the meantime, alongside the development of methods to synthesize ultrathin membrane materials over the past 10–15 years,[56–59] a new door opened for electron microscopy in liquid water. In particular, with modern microfabrication techniques it is possible to prepare mechanically robust, electron transparent membranes ranging from a few tens of nanometers to a few atoms thick—far thinner than those available 80 years ago—out of materials like silicon nitride and graphene.[60,61] Small volumes of liquid can be "sandwiched" or encapsulated between these membranes in a secure, watertight fashion and placed directly in an electron microscope for observation without freezing, drying, or fixation. This "modern" form of liquid-phase electron microscopy has begun to offer a
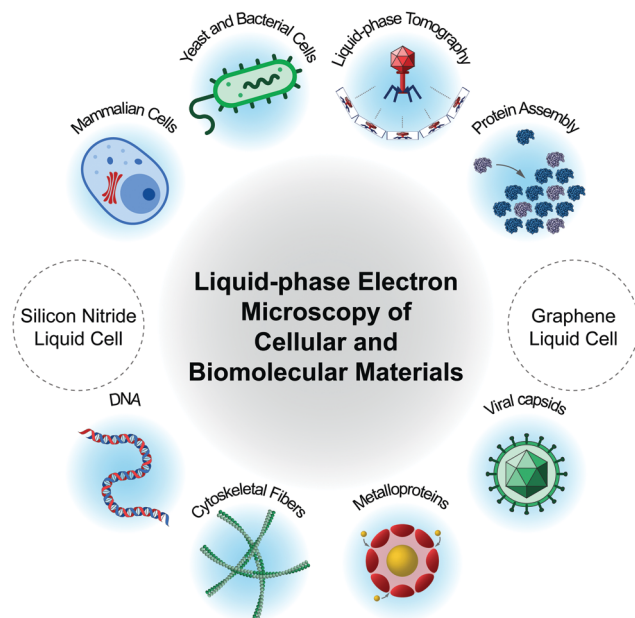
Fig. 1 Liquid-phase electron microscopy of biological systems, from cells to proteins. Through encapsulation between electron transparent membranes made of thin materials such as silicon nitride and graphene, liquid specimens can be examined in an electron microscope with near-atomic spatial and millisecond temporal resolution. This capability is opening up the potential for new biophysical investigations at many length scales.

valuable new lens into myriad phenomena in abiological and inorganic materials, including nanoparticle self-assembly,[62–65] atomic crystallization,[59,66,67] electrochemistry,[68–71] phase transitions,[70,72] nanoscale diffusion,[73–75] and recently certain polymeric systems,[76–78] with nanometer to atomic resolution.[60,61] These highly active research directions have been summarized in several recent reviews.[56,61,63,79–83] Here, however, we focus on a newer development: the application of liquid-phase electron microscopy tools to biological systems at various length scales, including ongoing efforts in whole cell imaging, studies of peptide assembly and aggregation, "single molecule" imaging, and related investigations (Fig. 1). Successes as well as experimental challenges for imaging these materials with liquid-phase electron microscopy are highlighted, along with potential routes to expand the capability of the technique to provide insight into molecular and biologically meaningful phenomena. We anticipate that such developments would establish liquid-phase electron microscopy as a powerful asset in the biophysicist's toolbox, able to provide new insight into the intricate biomolecular interactions, fluctuations, reactions, and functionality which drive life processes at the nanoscopic level.

2. Imaging electron-sensitive materials: resolution, radiolysis, and electron dose rates

Because of their overall low atomic number, small size, flexibility, and susceptibility to electron-induced damage, organic

and biological materials often pose a challenge for electron microscopy characterization, even in the absence of liquid. Overall, both high electron dose rates (high electron flux) and high cumulative electron doses—which might otherwise help improve resolution and the signal-to-noise ratio—can lead to irreversible damage of biological systems, through a combination of radiolysis (including in the surrounding liquid water medium, which generates reactive and damaging radicals that can go on to react with the specimen) and knock-on damage, or the direct displacement of atoms. The physical processes underlying these damage mechanisms have been reviewed elsewhere.[84–88] Other deleterious effects can include charging of the supporting substrate under sustained electron exposure, which can have both direct and indirect effects (e.g., induction of drift), excessive scattering from thick liquid layers, etc. For all the above reasons, it is imperative to minimize the exposure of biological specimens to the electron beam. In a liquid environment, an additional complication is that damaged species and the harmful products of electron-induced radiolysis are highly diffusive. For this reason, there have been several efforts in liquid-phase electron microscopy to build on the theory of resolution and electron beam effects from conventional and cryo-EM to understand the reaction–diffusion phenomena also at play under electron illumination in liquid.[69,70,89] These phenomena, as well as various means to combat or manipulate them, are discussed in detail below.

In an effort to understand electron beam-induced radiolysis in liquid semi-quantitatively, Schneider et al. undertook a theoretical modeling approach, considering the primary products of electron beam radiolysis (hydrated electrons, hydrogen and hydroxide radicals, dihydrogen, hydrogen peroxide, protons, and perhydroxyl radicals) and each of the known reactions that these species can undergo with each other and pure water.[69] Using reaction rate constants compiled from the literature and assuming instantaneous generation of the primary products once the electron beam is applied, they assembled a "complete" reaction diffusion system suitable for numerical analysis (Fig. 2a–c). In general, their results for deionized water indicate (i) the concentration of reactive species reaches a steady state extremely rapidly relative to experimental time scales (within a few milliseconds), with dihydrogen and hydrogen peroxide being the predominant products, (ii) the steady-state concentration of all species increases with increasing electron dose rate, and (iii) radiolysis species reach their normal, equilibrium concentration within a few microns of the outer edge of illumination. Result (ii) is of special note because dihydrogen can quickly reach its saturation concentration, which leads to the formation of bubbles in the liquid cell that can deform or otherwise deleteriously interact with "soft" biological specimens. In addition, the pH of the solution is generally decreased under electron illumination, which can have a significant effect on the protonation state of peptides and other molecules, and in turn disrupt the stability and activity of these specimens. Each of these behaviors, however, is sensitive to factors like the starting pH (Fig. 2c).

Besides illumination and pH conditions, radiolysis under electron illumination depends on additives in the solvent. With
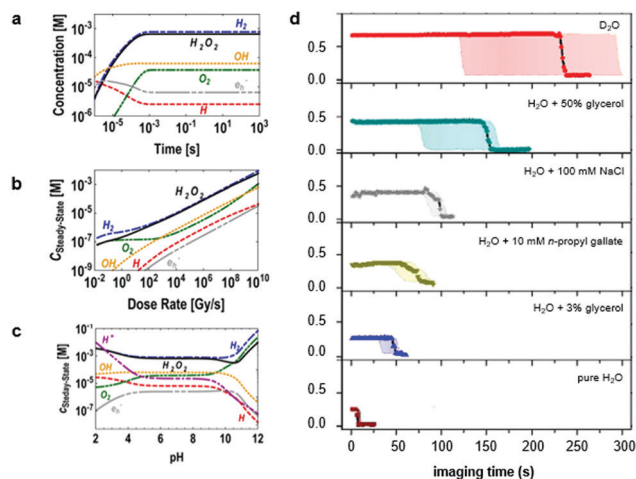
Fig. 2 Role of the chemical environment in liquid-phase transmission electron microscopy studies: generation of radiolysis species and the role of additives. (a) Electron irradiation of pure water generates a variety of radicals and reactive species, whose concentration based on numerical modeling is expected to reach a steady state within a few milliseconds of illumination. Note that H_2 and H_2O_2 are the most abundant species produced by this system of radiolysis reactions. (b) Steady state concentration of radiolysis products at neutral pH and various dose rates, and (c) a constant dose rate and various initial pH conditions. Reproduced with permission from ref. 68. Copyright 2014 American Chemical Society. (d) Experimental "bubble free time" of graphene-encapsulated water with different kinds of additives under electron illumination. For an accelerating voltage of 120 kV and an electron dose rate of 22 e⁻ Å⁻² s⁻¹, hydrogen bubbles were generated in pure water within a few seconds. However, addition of glycerol, gallate, sodium chloride, or deuterated water suppressed bubble formation, with the latter being most effective. Adapted with permission from ref. 85. Copyright 2018 American Chemical Society.

the proper selection of functional groups, this effect can serve as a handle to combat the effects of radiolysis estimated in the work of Schneider *et al.* (which only considered reactions in pure water),[69] or manipulate the environment such that the electron beam induces a desired phenomenon.[62,67,90–92] For example, Woehl and Abellan outlined the ability of a wide variety of additives to "scavenge" radiolysis products based on mutual reactivity.[93] Bromo, iodo, and thiol groups, for instance, were predicted to be excellent scavengers of hydrated electrons (with reaction rate constant $k > 10^9$ M⁻¹ s⁻¹), whereas alkenes and aromatic groups sequester hydroxyl and hydrogen radicals. One conceivable consequence of this phenomenon, with particular relation to biological systems, is that solution conditions under electron illumination may depend on the choice of buffer. It is possible that some may be more "protective" than others. For example, MOPS (3-(*N*-morpholino)-propanesulfonic acid) and HEPES (4-(2-hydroxyethyl)-1-piperazine-ethanesulfonic acid) are two common and similar biological buffers, but the former lacks an alcohol group which can react rapidly with hydroxyl radicals. However, these buffer nuances have not yet been tested experimentally. It is also worth noting that some buffers are empirically easier to encapsulate, particularly when it comes to graphene liquid cells, and so there may be tradeoffs involved. Another finding of this work were solution (and illumination) conditions which could be used to

promote overall reducing or overall oxidizing conditions, although these are more relevant to "hard" material liquid-phase electron microscopy, where they can be used to induce etching or deposition, for example.[67,90,91]

A second strategy to manipulate electron beam-induced solution chemistry is to change the solvent entirely and use heavy water (*i.e.*, D_2O, or deuterated water).[94,95] Heavy water has a radiolysis rate 1.1–1.5 times slower than regular water,[96] and therefore is expected to generate harmful species more slowly. This radiolysis suppression effect was recently shown experimentally, when Wang *et al.* found that, compared to additives like glycerol, heavy water can drastically increase the "bubble-free time" of graphene liquid cells illuminated with electrons[94] (bubbles are currently believed to consist of H_2/D_2 vapor generated by radiolysis). Using 120 keV electrons and a dose rate of 22 e⁻ Å⁻² s⁻¹, pure water graphene liquid cells were observed to have a bubble-free time of tens of seconds, whereas heavy water graphene liquid cells could be illuminated for hundreds of seconds before formation of bubbles due to radiolysis (Fig. 2d). It must be noted, however, that the structure and flexibility of biomolecules can be significantly altered in D_2O.[97,98] Hydrogen bonds involving deuterium are slightly different, which can disrupt enzyme active sites, inhibit assembly of structures like the delicate mitotic spindle in eukaryotes, *etc.*[99,100] Other non-buffer additives may also have tradeoffs; glycerol, for example, has been found to compact the structure of some proteins[101,102] and may have other effects, such as increasing the viscosity of the surrounding medium. Other additives may have specific interactions with proteins. In all, the protective potential of additives must be weighed against how they might impact the biophysical phenomena in question, if such chemicals are used.

In addition to the chemical environmental effects described above, radiolysis and resolution in liquid-phase electron microscopy also depend on a number of physical factors, especially the liquid thickness, but also the presence of interfaces, the choice of substrate material, *etc.* Regarding liquid thickness, inelastic scattering of the electron beam as it passes through windows or the solvent not only reduces overall imaging contrast; it also "spreads" the beam energy distribution (chromatic spread), both in scanning transmission electron microscopy (STEM) and transmission electron microscopy (TEM), which lowers the achievable resolution (Fig. 3a).[103–105] For example, de Jonge estimated that increasing the liquid thickness beyond ~100 nm rapidly degrades resolution, for both bright field and dark field imaging modes, due to excessive inelastic scattering. This beam broadening behavior in thick liquid layers carries its own set of experimental best practices. For example, in STEM mode, it is usually better to image phenomena taking place at the upper window of the liquid chamber, but for TEM mode, the theoretical resolution of phenomena at the lower window is higher.[80,103] Besides just changing focus, one way to implement this strategy is to functionalize only one of the windows (*e.g.*, a poly-L-lysine coating can be used to grow cells preferentially on one of the two windows[104]).

Another important consideration relates to the presence of interfaces in the liquid cell. In particular, in a follow-up to the
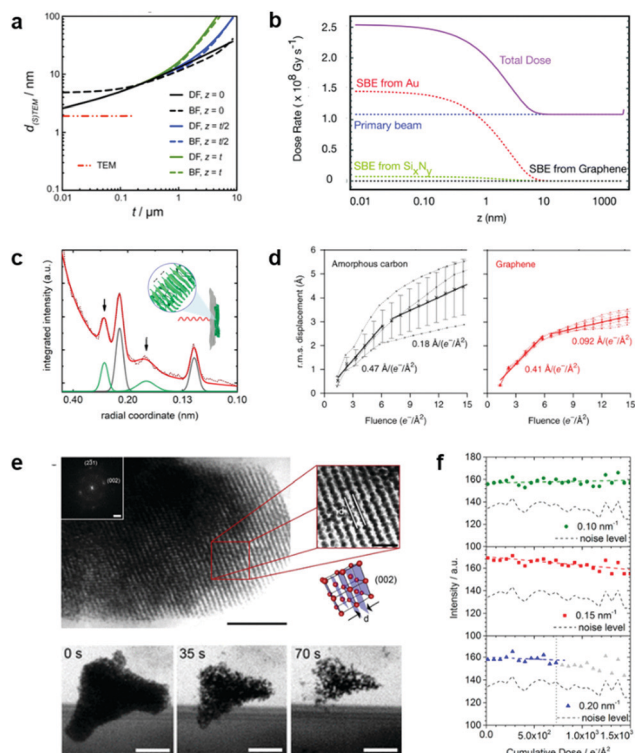
Fig. 3 Role of the physical environment in liquid-phase electron micro-scopy, including the impact of chamber thickness, window material, and the protective role of graphene. (a) Theoretical bright field (BF) or dark field (DF) imaging resolution for organic matter encapsulated in liquids of different thickness (*t*). In both modes, increasing the liquid thickness above ∼100 nm leads to rapid loss of resolution. Note that for organic matter, TEM outperforms STEM. Reproduced with permission from ref. 92. Copyright 2018 Elsevier. (b) The total effective electron dose can be increased through the generation of secondary and backscattered electrons (SBEs) near liquid chamber materials, such as gold (*e.g.*, in electrochemical cells) or even the silicon nitride membrane. Graphene, however, contributes essentially no SBEs, and may even serve as a sink for harmful species. Reproduced with permission from ref. 84. Copyright 2019 Royal Society of Chemistry. This protective potential of graphene has been evidenced in many TEM modalities, such as negative stain TEM (c) where it enables electron diffraction from miniscule protein bundles (Adapted with permission from ref. 45. Copyright 2019 American Chemical Society), and cryo-EM (d), where graphene has been shown to be much less susceptible to charging-induced drift relative to amorphous carbon (Reproduced with permission from ref. 95. Copyright 2019 National Academy of Sciences). Similarly, in liquid-phase TEM, gold nanoparticle DNA superlattices remained intact in graphene liquid cells (e, top) but were destroyed in the silicon nitride liquid cell at similar electron dose rates (e, bottom). Scale bar: 50 nm. Adapted with permission from ref. 96. Copyright 2017 American Chemical Society. (f) Microtubules in graphene liquid cells were also shown to retain high resolution details (∼5 nm resolution or better) even with cumulative doses in excess of 500 e$^-$ Å^{-2}. Reproduced with permission from ref. 97. Copyright 2018 American Chemical Society.

work of Schneider *et al.*,[69] it was suggested that the steady state behavior of radiolysis species in the vicinity of interfaces can be drastically changed through the generation of secondary and backscattered electrons (SBEs, Fig. 3b).[89] Through this process, materials including silicon nitride can act as an additional source of reactive species, and thereby increase the total effective dose in their vicinity. Graphene, however, not only

contributes negligibly to SBE generation, but, by virtue of its conductivity, may also serve as a radical scavenger.[89] This protective capability has indeed been observed experimentally, in vacuum, in vitreous ice,[106,107] and in liquid.[74,108,109] For example, although electron diffraction can involve subjecting materials to relatively high electron doses, the use of a graphene substrate allowed for the detection of structural information even from small, ∼30 nm protein "nanobundles" in negative stain electron microscopy (Fig. 3c).[45] Similarly, in cryo-EM, graphene substrates help suppress beam-induced substrate charging, which can cause drift of the specimen and loss of resolution (Fig. 3d).[106,107,110] Using graphene for liquid-phase electron microscopy experiments can be a challenge to put into practice, due to its out-of-plane fragility when the substrate is prepared or when pockets are formed. Thus there have been some recent efforts to make their prepara-tion more robust and reproducible (handling approaches,[111–113] synthesis routes to produce higher quality and single-crystalline graphene,[114] *etc.*). Nevertheless, the protective capabilities of graphene have also begun to be shown in liquid-phase TEM. For example, Cho *et al.* observed that, while gold nanoparticle–DNA superlattices encapsulated in graphene liquid cells could retain their structure at dose rates up to 250 e$^-$ Å^{-2} s^{-1} (Fig. 3e, top), even for several minutes, when the same structures were examined in silicon nitride liquid cells using the same illumina-tion conditions, they began to disintegrate within one minute (Fig. 3e, bottom).[108] However, coating the inner surfaces of the silicon nitride cell with graphene, or adding graphene oxide flakes to the solution, allowed these structures to be observed for longer times. In another study, encapsulating microtubules between graphene sheets was found to preserve structural information at resolutions of 5 nm or better, even after a total accumulated dose in excess of 500 e$^-$ Å^{-2} (Fig. 3f).[115] In this investigation, the protective capability of graphene was suggested to exceed even that achieved through the use of cryogenic temperatures. In short, although quantitative and mechanistic understanding of these various protective effects is still being developed, graphene windows and overall thinner liquid pockets can be advantageous for multiple reasons.

3. Liquid-phase electron microscopy, from cells to molecules

3.1. Whole cells

The study of intracellular dynamics has long been the domain of optical microscopy, with electron microscopy historically used to examine the overall ultrastructure of fixed and stained cells (the morphology and distribution of organelles, cell–cell adhesions, the cytoskeleton, *etc.*).[116,117] However, as discussed above, a number of dynamic cellular processes are beyond the reach of optical imaging methods. As such, and given their size, whole cells were among the earliest biological materials examined with liquid-phase electron microscopy[56,104] and, to date, pheno-mena including the dynamic distribution of membrane proteins,[79,104,118] the surface localization of viral particles,[119,120]

and the behavior of metallic nanoparticles at cell peripheries[121] have been studied. Although eukaryotic cells tend to be much larger (and thus more difficult to penetrate with an electron beam), they have been the predominant targets. In such investigations, contrast is often improved through the use of metallic nanoparticle or quantum dot labels on features of interest. While this strategy is reminiscent of super-resolution optical microscopy methods, at least one major advantage of liquid-phase electron microscopy is that nanoparticles do not need to be as sparsely distributed, so clustering, stoichiometry, and other behaviors of labeled features are readily accessible at 3–5 nm spatial resolution and relatively high temporal resolution.[104,118] Whole cell liquid-phase electron microscopy has also seen the greatest use of correlative characterization (mainly alongside fluorescence microscopy),[109,122,123] as discussed in more detail below.

3.1.1. Eukaryotic cells. The majority of whole-cell liquid-phase electron microscopy investigations have considered eukaryotic cell types. These include COS7 fibroblast cells,[79,104] Madin–Darby canine kidney (MDCK) cells,[109] SK-BR-3 breast cancer cells,[79,118] PC3 and LNCaP prostate cancer cells,[124] glioblastoma stem cells,[121] and yeast cells.[125] In general, eukaryotic cells are much larger than bacteria (>5 μm), and so it is challenging to penetrate their thickest regions—like in the vicinity of the nucleus—using reasonable electron doses in conventional TEM without first washing away the cell membrane.[109] For this reason, STEM has been used more often for such studies, and sometimes further supplemented by nanoparticle or quantum dot labels on specific features of interest to achieve improved signal-to-noise (*i.e.*, through atomic number, or *Z*-contrast). However, unlabeled eukaryotic cells have been imaged successfully with TEM when graphene liquid cells were used,[109] or if the focus is on phenomena at the much thinner cell edge.[121]

In what was one of the first modern liquid-phase electron microscopy studies of biological materials, de Jonge *et al.* used liquid-phase STEM to examine the distribution of epidermal growth factor receptors (EGFRs) in COS7 fibroblast cells.[104] They grew fibroblasts directly on a poly-L-lysine-coated silicon nitride window, which allowed preferential adherence to one side of the liquid chamber, and then incubated these cells with EGFRs labeled with 10 nm gold nanoparticles for various durations before sealing the silicon nitride chamber and inserting it into the microscope for imaging. As expected, cells incubated with gold-labeled EGFRs for a short time (5 min) exhibited a mostly random distribution of labeled EGFRs, and clusters of at most 2–9 nanoparticles/EGFRs (Fig. 4a). However, when the same receptors were incubated with cells for 10–25 min, larger and roughly circular clusters were observed, which the authors attributed to incorporation into round intracellular endosomes (Fig. 4b). The overall resolution of their results was estimated to be about 4 nm and, using a theoretical model based on the balance between elastic and inelastic scattering in the liquid chamber, it was proposed that nanoparticles as small as $\sim$2 nm could be detected and localized with liquid-phase STEM in a chamber several microns thick. Later, using a similar approach (but using quantum dot-labeled affibodies targeting the HER2 receptor in SK-BR-3 breast cancer cells), the authors
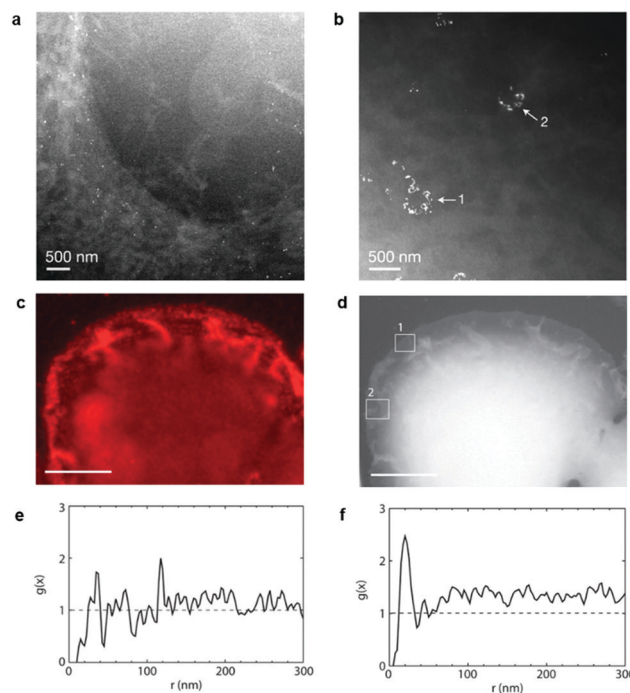

Fig. 4 Liquid-phase electron microscopy of whole eukaryotic cells. (a and b) COS7 fibroblast cells incubated with nanoparticle-labeled EGFR for 5 min (a) and 10–25 min (b) as visualized with liquid-phase STEM. The distribution of EGFRs was initially observed to be random but after longer incubation, circular clusters were observed, and attributed to internalization of the receptors in endosomes. Reproduced from ref. 93. Copyright 2009 National Academy of Sciences. (c–f) Quantum dot-tagged HER2 receptors on SK-BR-3 breast cancer cells visualized by fluorescence microscopy (c) and STEM (d). Fluorescence microscopy revealed a subpopulation of cells exhibiting "ruffled" and "unruffled" regions. Quantification of the HER2 distribution in STEM revealed that these regions had distinct organization of HER2. Unruffled regions (box 1 in panel d) exhibited a random distribution of HER2 (on the basis of the radial distribution function shown in e), whereas ruffled regions (box 2 in d) tended to exhibit a high degree of HER2 dimerization (on the basis of the radial distribution function shown in f). Scale bars: as indicated and 10 μm for (c) and (d). Adapted with permission from ref. 103. Copyright 2015 American Academy of Arts and Sciences.

demonstrated a more surprising result.[118] HER2 receptors are believed to be key players in breast cancer progression, and their differential expression and organization across and among cells is associated with metastatic potential but is not well understood. In their correlative optical microscopy–liquid STEM investigation, fluorescence and phase contrast microscopy revealed that SK-BR-3 cells had either flat or "ruffled–unruffled" morphologies. Following this observation, precise localization of the quantum-dot labeled receptors in STEM enabled the authors to show quantitatively that the clustering/dimerization of HER2 was different in each of these regions (Fig. 4c and d). "Ruffled" regions in "ruffled–unruffled" cells tended to exhibit a high degree of HER2 homodimerization and labeling density, whereas "flat" cells appeared to completely lack HER2 homodimers, and instead exhibited a more random HER2 distribution (Fig. 4e and f). It was proposed that this heterogeneity of protein expression could be linked with drug resistance mechanisms and metastatic potential.[118]

In a related study using liquid-phase TEM, rather than STEM, Pohlmann *et al.* monitored the distribution of gold nanorods at the periphery of glioblastoma stem cells (Fig. 5a).[121] Gold nanoparticles are attractive both as bioimaging contrast agents (at larger scales) and as potential drug delivery systems, but their interactions with cell membranes at the nanoscopic level—the critical first step for cellular internalization—is not well understood. Pohlmann *et al.* first grew glioblastoma stem cells enriched with the NOTCH1 receptor to attach them to custom silicon nitride microwells by immunoaffinity capture. Gold nanorods coated in polyvinylpyridine were then added before sealing the microwells, and imaged with an accelerating voltage of 120 keV and low electron dose rates ($0.5 \, e^- \, \text{Å}^{-2} \, s^{-1}$). Nanorods were observed to be concentrated near the cell periphery and, in some cases, the nanorods "inside" the cells but still near the membrane exhibited diffusive motion (Fig. 5a, right). Surprisingly, glioblastoma cells were observed to "retract" in response to more dilute nanorods solutions, across multiple experiments, which was attributed either to beam damage or cytotoxicity (although *ex situ* cell viability assays showed little cytotoxicity from the nanorods). Overall, however, this study showed that real-time visualization of nanoparticles alongside single cells could be achieved using TEM, as well as STEM.

Whole cells have also been imaged without the use of nanoparticles, using thinner cell types (such as yeast) or thinner windows/chambers (*e.g.*, graphene). For example, Peckys *et al.* were able to study the behavior of various strains of *Schizosaccharomyces pombe* (wild type and a series of three mutants) in liquid-phase STEM.[125] Compared to their previous experiments using nanoparticle labels, which achieved resolutions between 3 and 5 nm,[79,104,118] these studies only achieved a resolution of ∼30 nm using a cumulative electron dose of about 0.22 $e^- \, \text{Å}^{-2}$. However, this resolution was sufficient to reveal structures like the cell wall (0.1–0.2 μm thick), primary and secondary septa, at least two types of intracellular vesicles, *etc.* Using Monte Carlo simulations to estimate the contrast of different possible cellular components, the authors proposed that "light" vesicles may have corresponded to dense peroxisomes, whereas "dark" vesicles may have corresponded to lipid droplets. The various yeast mutants under investigation were also shown to exhibit distinct behaviors (*e.g.* "chaining" of spn3Δ mutants undergoing division) and morphologies (orb-25 mutants were rounder than wild type *S. pombe*). Park *et al.*, meanwhile, used graphene liquid cells to encapsulate unlabeled MDCK cells for investigation (Fig. 5b–g).[109] For mechanical stability, either multilayer (3–10 layer) graphene was used, or a combination of a graphene top membrane and a silicon nitride bottom membrane. The MDCK cells were cultured on either substrate and, after verifying their presence with fluorescence microscopy (Fig. 5b), imaged in TEM mode at 120 kV (Fig. 5c). Due to the low background scattering of graphene, they were able to use lower electron doses than previous studies.[104] The same cells were then reexamined under fluorescence microscopy, to validate their overall structural integrity (Fig. 4d). In some cases, the contrast was further improved by fixing the
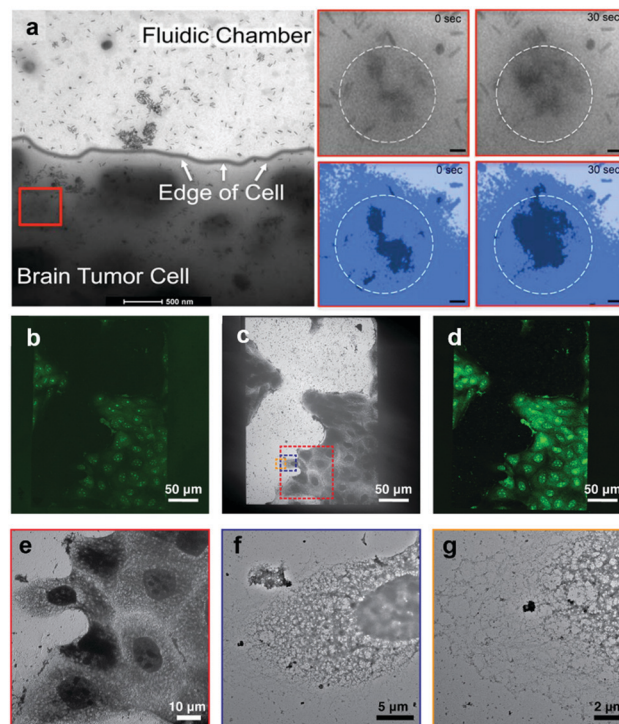

Fig. 5 Glioblastoma cells and MDCK cells imaged in silicon nitride and graphene liquid cells, respectively. (a) Low-magnification view of gold nanorods incubated with glioblastoma stem cells in a silicon nitride liquid cell. Nanorods within the cell were observed to diffuse dynamically (right) across tens of seconds. Adapted with permission from ref. 106. Copyright 2015 American Chemical Society. (b–g) Sequential observation of MDCK cells by fluorescence microscopy and electron microscopy. Panels (b) and (d) were taken before and after electron microscopy examination. (e–g) Progressively magnified views of the boxed regions (red to blue to yellow) in (c). These MDCK cells had been stripped of their cytoplasm by detergent treatment, but the cytoskeletal structure is visible in great detail. Scale bars: as indicated and 50 nm (b). Adapted with permission from ref. 100. Copyright 2015 American Chemical Society.

cytoskeletal structure with phalloidin, washing away the cell membrane with detergent, and then encapsulating the specimen between graphene sheets. In these cases, fine details of the cytoskeletal structure could be resolved (Fig. 5e and f).

3.1.2. Prokaryotic cells. The smaller number of prokaryotic cell studies in liquid-phase electron microscopy have focused primarily on interactions between bacteria and viruses, such as bacteriophage P1 or the flagellotropic phage 7-7-1 (Fig. 6).[119,120] For example, Kennedy *et al.* studied AW405 and K12 *E. coli* cells incubated with P1 phage using liquid-phase STEM. To improve imaging contrast without nanoparticle labels, using *ex situ* live/dead assays they first estimated the amount of uranyl acetate—a common biological stain that provides *Z*-contrast—for which *E. coli* cells could remain viable in a minimal phosphate medium. These experiments suggested that at least 90% of *E. coli* cells remained intact in environments with ≤0.1% uranyl acetate. Moving forward, *E. coli* cells stained with 0.1% uranyl acetate were imaged in liquid-phase STEM at various doses between 0 and 0.8 $e^- \, \text{Å}^{-2}$ per frame before post mortem analysis. These experiments suggested that the median lethal electron dose for
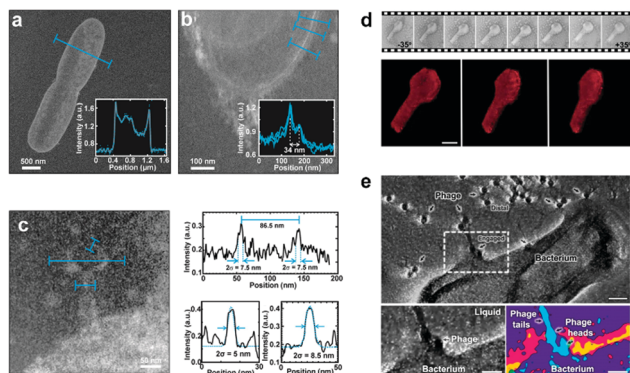
Fig. 6 Liquid-phase electron microscopy and tomography of *E. coli* cells and viruses. (a and b) At slightly high dose (above the median lethal dose estimated in ref. 104), inner and outer membranes of *E. coli* cells can be discerned with the use of light positive staining with uranyl acetate (0.1%). Details of P1 bacteriophage can also be visualized (c), *e.g.*, based on intensity line-scans, the head diameter and thickness, and the stalk thickness. Adapted with permission from ref. 104. Copyright 2016 American Chemical Society. (d) Tilt series and segmented area of flagellotropic phage 7-7-1 acquired through liquid cell electron tomography. (e) Overview and zoomed-in view of a phage interacting with a hydrated *E. coli* cell. Adapted with permission from ref. 105. Copyright 2019 American Chemical Society. Scale bars: as indicated and 50 nm (d), 500 nm (e, top), 15 nm (e, bottom).

E. coli under these conditions is around 0.3 e⁻ Å⁻² for 300 keV electrons (although elsewhere it was argued that more rigorous routes should be taken to estimate the lethal dose[126,127]). Unfortunately, few details of the *E. coli* cells could be discerned at such a dose, but with an illumination of 0.66 e⁻ Å⁻², it was possible to make out inner and outer cell membranes, flagella, and other features (Fig. 6a and b). Movement of the P1 bacteriophage at the cell boundary was also observed, at a dose rate of 0.16 e⁻ Å⁻² per frame (Fig. 6c). Notably, the tail sheath of the virus in projection appeared to "contract," but at the demonstrated resolution it is difficult to decouple this observation from overall rotation or diffusion of the virus due to Brownian motion in three dimensions.

In their study, Dearnaley *et al.* devised an innovative way to investigate cell–virus interactions in three dimensions, using liquid cell electron tomography.[120] In tomography, a series of two-dimensional projections are collected from several different viewing angles and used to reconstruct mathematically a three-dimensional volume.[128–130] Normally, the geometry of the silicon nitride liquid cell makes it difficult to reach a sufficient range of tilt angles to achieve a full 3D reconstruction. To overcome this limitation, Dearnaley *et al.* developed a "hybrid" chamber composed of a silicon nitride microchip and a collodion/carbon-coated TEM grid. Using this set-up they collected images of a flagellotrophic phage (Fig. 6d) and of the same phages associated with *Agrobacterium* sp. H13-13 (Fig. 6e) from various perspectives (±35°). Interactions between phages and the bacterium in various orientations, both along the cell body and near flagella, were revealed. It is notable that graphene liquid cells may also be able to accommodate a high range of tilt angles. However, regardless of whether silicon nitride or graphene liquid cells are used,

it is important to consider that this method assumes that the features to be reconstructed are essentially static for the time scale over which each individual tilt series is collected. Thus, the achievable spatial resolution is governed not only by the imaging set-up and the accessible range of angles, but also the length scales at which the structure in question may have changed or moved during tilt series acquisition. This motion could include any normal, Brownian rotation of the specimen as it is in liquid, which would make tilt series alignment more of a challenge. Were several tilt series over time to be collected, a similar caveat applies to temporal resolution. Similarly, tomography specimens accumulate a significant total electron dose in the process of collecting a tilt series (generally several tens of images are required).

In a very recent study, Koo *et al.* used hybrid silicon nitride–graphene liquid cells to image the morphology of various bacterial cells (*Escherichia coli*, *Lactococcus lactis*, and *Bacillus subtilis*).[131] In this correlative study, the cells were supported on the silicon nitride chip and "blanketed" with graphene before being imaged with fluorescence microscopy, scanning electron microscopy, or atomic force microscopy. After overall morphological examination of each cell type, they evaluated the growth of *E. coli* which had been subjected to electron exposure of various durations and with and without the graphene blanket. These experiments provided evidence that cells can proliferate after being exposed to as many as 3×10^8 10 keV electrons per cell when blanketed by graphene, but could sustain two orders of magnitude or fewer electrons when not covered, another experimental validation of the protective potential of graphene.

3.2. Protein crystallization, peptide assembly, and pharmaceutical aggregation

Understanding how proteins and peptides assemble and aggregate at the nanoscopic level is critical for both fundamental science and technological applications. For example, insight into the molecular scale dynamics of proteins as they crystallize could aid X-ray and electron crystallography studies, which are often limited by difficulties in preparing large and ordered protein crystals. Despite this challenge, these tools remain indispensable for probing the atomic scale structure of biological materials.[21,50,132] Such knowledge could also suggest novel ways to grow synthetic assemblies, made of polymers,[133,134] nanocrystals,[63,64,135] *etc.* Understanding the nuances of nanoscale protein interactions in liquid could also lead to strategies to improve the stability of peptide-based drugs and therapeutics,[136,137] aggregation-prone proteins,[45,138] and more. Several recent liquid-phase electron microscopy investigations (mostly TEM) in this vein are summarized in more detail below.

3.2.1. Peptide assembly and protein crystallization. The protein lysozyme readily crystallizes into a variety of structures depending on solution conditions, and has therefore become a model system both for fundamental studies of protein crystallization[139,140] and for testing new electron imaging and diffraction techniques.[132,141,142] In two studies, Yamazaki *et al.* were able to use low-dose liquid-phase TEM to study nanoscale nucleation, growth, and defect annealing in individual
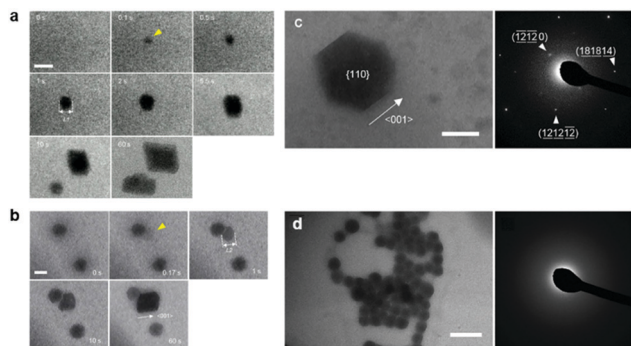
Fig. 7 Nucleation and growth of lysozyme crystals visualized by liquid-phase TEM. (a and b) Crystal nucleation was observed to be heterogeneous, occurring either on the silicon nitride substrate (a) or from the surface of dense amorphous aggregates. (c and d) The structure of the crystalline (c) and amorphous (d) phases was verified by electron diffraction; amorphous aggregates show only "rings", indicating a lack of long-range order. Scale bars: 200 nm (a–c), 500 nm (d). Reproduced from ref. 125. Copyright 2017 National Academy of Sciences.

lysozyme crystals (Fig. 7).[141,142] For example, using silicon nitride liquid cells and electron dose rates less than 3.2 e$^-$ Å^{-2} s^{-1}, the authors observed the formation of two types of structures: ordered lysozyme crystals (Fig. 7a, as evidenced by the diffraction pattern in Fig. 7c) and dense, amorphous lysozyme clusters (Fig. 7b, as evidenced by a ring-like diffraction pattern in Fig. 7d).[141] In a conventional two-step crystallization pathway,[64,143,144] such amorphous clusters would be expected to serve as a medium or precursor for the formation of a dense and ordered, final crystal form. However, in their experiments, Yamazaki et al. did not observe the formation of crystals in the interior of such clusters; instead, lysozyme crystals were nucleated heterogeneously, either directly on the silicon nitride substrate (Fig. 7a) or on the surface of the amorphous clusters (Fig. 7b). At 3.2 e$^-$ Å^{-2} s^{-1}, these crystals grew continuously, but if the electron dose rate was increased to 290 e$^-$ Å^{-2} s^{-1}, the crystals became damaged and dissolved. In a follow-up study,[142] the authors examined the diffusion of defects in much larger lysozyme crystals. Surprisingly, void-like features tens of nanometers in size within large, faceted crystals had high mobility, indicating that crystal bonds can rapidly rearrange and exchange to anneal out defects. It was proposed that, especially in small crystals, such defect mobility could lead to large scale reconfiguration, even to the extent of solid–solid phase transitions.

In a more recent study, Touve et al. used liquid-phase TEM to investigate cyclic and linear peptides which assemble either inherently (the case for linear peptides) or after covalent modification (the case for cyclic peptides).[145] A significant portion of this work was devoted to assessing the impact of the electron beam, through a series of post mortem characterization experiments using matrix assisted laser desorption ionization mass spectrometry (MALDI-MS). In particular, the authors collected MALDI spectra from unilluminated, chamber-bound peptides and from peptides which had been illuminated in liquid chambers with various electron dose rates (0.1–30 e$^-$ Å^{-2} s^{-1}), for various durations (0 to ~50 min) and with various illumination patterns (1 s pulses every minute or continuous illumination).

In general it was observed that either low dose, pulsed, or low dose + pulsed illumination could preserve the integrity of the linear peptide for at least 30 minutes, whereas both pulsed and low dose illumination was required to preserve the cyclic one. Using the latter condition, the authors then induced assembly of the cyclic peptide by introducing either tris(2-carboxyethyl)-phosphine (TCEP) or the enzyme thermolysin, which linearize the peptide and allow it to assemble (Fig. 8). Both ex situ and in situ (both on silicon nitride substrates), early stages of peptide assembly were indicated, ~11 min after adding TCEP or ~25 min after adding thermolysin. The expected ribbon and sheet-like structures were not observed, but this result was attributed either to (i) the lack of buffering salt in the medium or (ii) strong interactions between the peptides and the silicon nitride substrate, which would frustrate proper assembly. Notably, assembly of the cyclic peptide under liquid-phase TEM was not observed in control experiments where thermolysin was not added to the mixture, indicating that the enzyme at least partially maintained its bond-cleaving activity in these experiments.

3.2.2. Protein aggregation and phase-separation. Peptide and protein aggregation into disordered structures are also important phenomena, with relevance to the stability of peptide-based pharmaceuticals, the partitioning of biomolecules
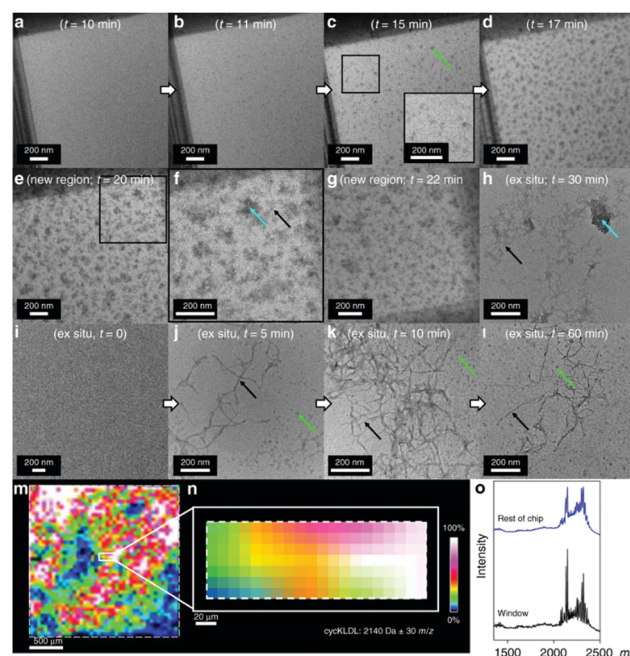

Fig. 8 Assembly and aggregation of peptides visualized by liquid-phase TEM in silicon nitride chambers and ex situ. (a–d) Liquid-phase TEM snapshots of cyclic peptide and TCEP under low dose, pulsed conditions. Assembly into dense aggregates was observed in the pure water conditions used for liquid-phase TEM. (e–g) Other views of the same liquid cell from regions which had been not been previously irradiated, demonstrating similar assembly in presumably undamaged areas. (h–l) Morphology development of peptide assembles which were assembled ex situ in a test tube before application to the silicon nitride window. (m and n) Post mortem MALDI-MS imaging of the silicon nitride window shown in (a–g). (o) Averaged MALDI spectrum of the region highlighted in (n) and from the whole chip. Reproduced from ref. 129.

into cellular droplets by liquid–liquid phase separation (a.k.a. coacervation), and different types of pathogenic protein aggregation. These phenomena have seen the greatest experimental attention in the form of ensemble spectroscopy or optical microscopy experiments,[137,138,146,147] but the heterogeneous processes occurring at the nanoscale remain poorly understood. In this regard, liquid-phase electron microscopy studies in this field are beginning to appear. For example, DiMemmo et al. used silicon nitride liquid cells to investigate the aggregation behavior of PEGylated Interferon α_{2a} (a.k.a. Pegasys®, by Roche), a commercial drug conjugate, under various environmental conditions (pH changes, temperature changes, etc.).[136] Their observations showed that, especially in response to high temperature (50–60 °C), Pegasys® could form large, amorphous protein aggregates. These aggregates, suspended in HEPES buffer, could be discerned migrating in liquid chambers with and without the use of staining at 120 kV, and many were observed to increase in size within 40 s. In some cases, aggregate chains formed, which, based on ex situ experiments, were proposed to influence immune protein clustering and aggregation.

Meanwhile, le Ferrand et al. studied the phase separation of histidine-rich beak protein 2 (HBP-2), a self-coacervating protein that, under particular solution conditions, condenses into ∼1 μm droplets through hydrophobic interactions.[148] By combining stain-free, real-time liquid-phase TEM observations with ensemble tools like circular dichroism spectroscopy and dynamic light scattering, they were able to follow the liquid–liquid phase separation of HBP-2 at various ionic strengths and initial protein concentrations. First an experimental phase diagram of HBP-2 was determined ex situ, and high salt conditions, or pH conditions near the isoelectric point of HBP-2, were shown to produce dense HBP-2 droplets after a brief lag time. These conditions were selected for dynamic liquid-phase TEM observation. At relatively high ionic strength (0.125 M NaCl), for example, dense droplets hundreds of nanometers in diameter were observed in liquid-phase TEM to grow continuously, whereas at a lower ionic strength (0.1 M NaCl), dense droplets would grow but then "dissolve", presumably as a result of transient interactions, into small oligomeric units. In the high ionic strength regime, cluster growth followed an approximately diffusion-limited form, with a power law of $\sim t^{0.61}$.

3.3. Single molecules and single proteins

Perhaps the ultimate goal in liquid-phase electron microscopy of biological systems is to push spatial and temporal resolution to their limits, and observe simultaneously the structure and dynamics of individual, hydrated proteins or biomolecules. Such a capability would offer an unprecedented lens into nanoscale biophysics, and help bridge knowledge gaps on interrelations between structure, dynamics, and function occurring at the molecular level. Several promising studies, especially those using graphene liquid cells for improved sample protection and signal-to-noise, have begun to push this limit and image individual viruses,[149,150] ferritin molecules,[151] cytoskeletal structures, and even DNA[74,95] in a liquid environment.

3.3.1. Cytoskeletal fibers. Cytoskeletal fibers, such actin bundles, microtubules, etc., were among the first protein structures observed with liquid-phase TEM, perhaps in part due to their readily identifiable anisotropic shape and periodic features (e.g., helical symmetry). For example, as early as 2012, Mirsaidov et al. encapsulated acrosomal actin bundles in silicon nitride liquid cells for imaging (Fig. 9a–c).[152] Fourier enhancement of the periodic features in these bundles allowed them to visualize the helical repeat unit comprising the bundles with approximately 2.7 nm resolution (Fig. 9c), using 120 keV electrons and a cumulative dose of 35 e⁻ Å⁻². In a similar study, but using graphene liquid cells, Keskin et al. examined the structure and beam sensitivity of microtubules.[115] Both these investigations used Fourier-domain analysis in an effort to understand the stability of their respective liquid specimens under the electron beam (Fig. 9d–f). For example, in the latter study, Mirsaidov et al. tracked the decay of high resolution features in response to accumulated electron doses between 0 and 80 e⁻ Å⁻² s⁻¹, for both silicon nitride liquid cell TEM and cryo-EM at 120 or 400 kV. Surprisingly, periodic features observed at 2.7 and 5 nm appeared to decay much more slowly at room temperature in liquid compared to at 98 K in vitreous ice, regardless of the accelerating voltage used.[152] The origins of this phenomenon are still under investigation. On the other hand, graphene's hypothesized protective capabilities were evidenced in the study by Keskin et al.[115] They also tracked the decay of high resolution features for increasing accumulated electron doses. Here, details of 5 nm or smaller in size could be perceived, even for accumulated doses in excess of 500 e⁻ Å⁻² (Fig. 9d, see also Fig. 3f). This behavior was compared to results from cryogenic conditions in the absence of graphene. In this case, for the same electron dose rate conditions, it was observed that graphene-encapsulated microtubules could sustain a greater accumulated dose before the onset of detectable damage relative to unsupported microtubules in vitreous ice (Fig. 9f). This behavior was observed for a range of electron dose rates, with the most significant effect being observed in the lower dose rate regime.

3.3.2. Viral particles and ferritin. Large protein structures, such as viruses, or protein structures containing high atomic number elements, such as ferritin and other metalloproteins, are also natural candidates for single-protein liquid-phase electron microscopy studies because they can exhibit high contrast against the liquid background. These two classes of proteins have indeed been the subject of a number of liquid-phase TEM investigations. For example, as early as 2012, Gilmore et al. demonstrated an affinity capture device to secure icosahedral rotavirus double layer particles (DLPs) in silicon nitride liquid cells.[149] These affinity capture systems involve coating the silicon nitride membrane with a small fraction of nickel–nitrilotriacetate (Ni–NTA)-functionalized lipids, followed by histidine-tagged protein A as an adaptor to polyclonal antibodies for the DLPs (Fig. 10a). Tethering the viruses in this fashion restricts translational and rotational motion, but at the same time this limits blurring of the specimen due to Brownian motion. A low concentration of contrast agent (uranyl formate) enabled the DLPs to be viewed in excellent detail, even at a dose
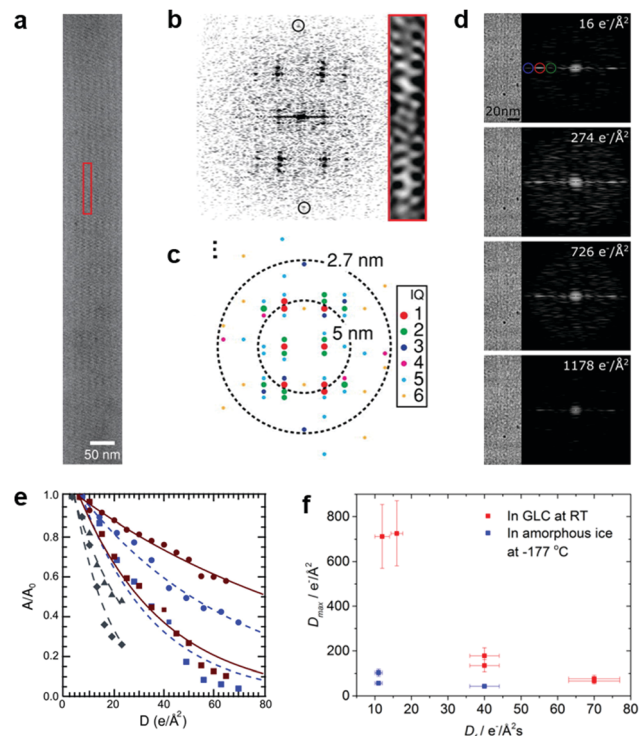
Fig. 9 Liquid-phase TEM of cytoskeletal structures, including (a–c) acrosomal bundles and (d) microtubules. (a) Large acrosomal bundles were imaged in the silicon nitride liquid cell with, on the basis of Fourier analysis (b), approximately 2.7 nm resolution. Enhancement of the periodic features in the 2D Fast Fourier Transform (FFT) allowed visualization of the actin helices making up the bundle (regions boxed in red in a and b). (c) "Integer quality" plot (IQ plot) of the FFT in (b), showing the relative intensity of different reflections relative to the noise level. The highest resolution reflection with signal-to-noise ratio greater than 2 was at 2.7 nm resolution. Adapted with permission from ref. 136. Copyright 2012 Elsevier. (d) Microtubule filaments visualized in graphene liquid cells at various cumulative electron doses. The decay of features in the 2D FFT patterns was attributed to accumulation of electron beam damage. Adapted with permission from ref. 97. Copyright 2018 American Chemical Society. (e) Intensity of Fourier features coming from acrosomal bundles at various accumulated doses, D. Squares denote 2.7–5 nm resolution features, circles denote features >5 nm. Triangles denote 2.2–3.7 nm resolution, and diamonds denote features >3.7 nm. Red, blue, and gray refer to room temperature liquid phase imaging, cryogenic imaging at 120 kV, and cryogenic imaging at 400 kV, respectively. (f) Comparison between D_{max}, the cumulative dose at which damage was first detected, and D_f, the electron dose rate, for microtubules imaged in unsupported ice at cryogenic temperatures (blue) and at room temperature in graphene cells (red). In these experiments, damage was detected at a much greater cumulative dose in the graphene liquid cells.
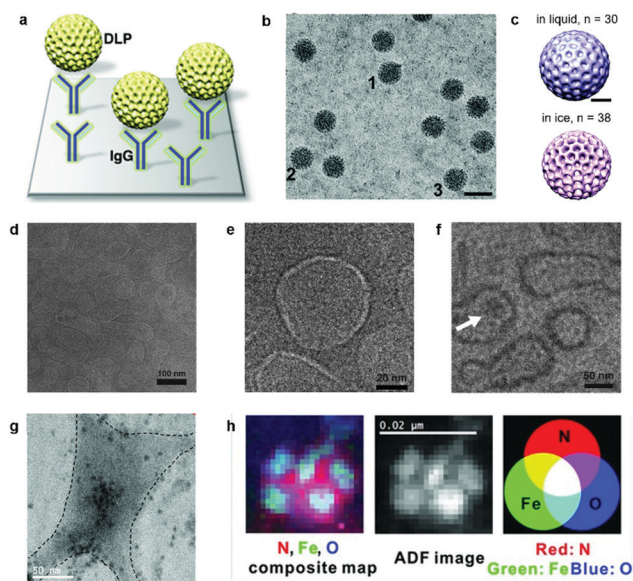

Fig. 10 Liquid-phase electron microscopy of individual viral particles (a–f) and ferritins (g and h). (a) Affinity capture scheme to secure double layer particles to the silicon nitride window. (b) Corresponding snapshot of double layer particles in liquid. (c) Cryo-EM reconstruction routines based on the icosahedral symmetry of the virus were used to compare the resolution achieved in liquid to the resolution achieved in ice. Adapted with permission from ref. 133 and 134. Copyright 2015 Royal Society of Chemistry. (d) Low-magnification and (e and f) high-magnification views of H3N2 virus encapsulated in graphene liquid cells. The white arrow in (f) indicates a denser region which may correspond to internalized genetic material. Adapted with permission from ref. 100. Copyright 2015 American Chemical Society. (g) Low-magnification view of ferritin encapsulated in a graphene liquid cell. The ~8 nm features correspond to the dense, iron oxide hydroxide cores of ferritin. (h) Elemental map of nitrogen, iron, and oxygen achieved through EELS and the corresponding annular dark field (ADF) image. Adapted with permission from ref. 135. Copyright 2014 John Wiley and Sons. Scale bars: as indicated and 100 nm (b), 30 nm (c).

of 5 e$^-$ Å^{-2} (Fig. 10b). The resolution in these studies was significant enough that, with enforcement of icosahedral (60-fold) symmetry, ~2.8 nm resolution three-dimensional reconstructed models could be generated using standard cryo-EM routines (Fig. 10c). In a similar study, Varano et al. used this DLP affinity capture system to achieve real-time imaging, and were able to capture some degree of lateral displacement over time, in some cases with hints of what were proposed to be ~8–21 nm stretches of viral mRNA visible on the virus exterior.[150] Meanwhile, Park et al. were able to examine the structure of H3N2 influenza

viruses using graphene liquid cells and without the use of contrast-enhancing agents.[109] Following encapsulation between multilayer graphene sheets, the shells of H3N2 viruses were readily visible at 120 kV using highly defocused conditions (up to 3 μm) and a dose of ~5 e$^-$ Å^{-2} per image (Fig. 10d–f). Continuous imaging of the viruses, however, led to contrast reduction and eventual degradation, even in graphene liquid cells.

Metalloproteins such as ferritin are generally smaller than viral capsids but contain heavy metal components which provide atomic number contrast in electron microscopy. Taking advantage of this, Wang et al. imaged ferritin encapsulated in single-layer graphene liquid cells with STEM operating at 80 kV for improved contrast.[151] They were able to observe high-contrast, ~8 nm features corresponding to the electron dense iron oxide hydroxide core of ferritin (Fig. 10g). These individual protein complexes could only be trapped in extremely thin liquid pockets, which, alongside bubble formation, inhibited dynamics studies, but at the same time enabled spectroscopic investigation of the iron oxide hydroxide core using electron energy loss spectroscopy (EELS). This technique was used to map the distribution of nitrogen, oxygen, and iron sandwiched between

graphene (Fig. 10h). In some cases, it was also possible to evaluate differences in the oxidation state of iron based on quantification of the Fe L-edges (*i.e.*, by comparing the width, intensity, and relative positions of the L_2 and L_3 emission peaks,[153,154] which represent transitions to empty d orbital states). However, these EELS studies demanded extremely high dose rates (10^6 e$^-$ Å^{-2}) in order to achieve sufficient signal to noise, which were shown to destroy the protein components of ferritin despite graphene's protective capabilities.

3.3.3. Nucleic acids. The fluctuations, self-assembly, and stability of nucleic acids like DNA and RNA are critical for the proper replication and storage of genetic information in living things. While some nucleic acid molecules are long enough for their dynamics to be studied using fluorescence microscopy (λ-DNA, large bacterial plasmids, *etc.*),[155–157] it is much more difficult to image DNA and RNA at the nanometer level, where their mechanics, inter- and intramolecular interactions, and fluctuations are more complex. Nevertheless, although DNA is much smaller than proteins like ferritin and viruses (the double helix has a diameter of just 2 nm), a high negative charge density and the stability of the phosphodiester bonds which form the DNA backbone have made it possible to study different properties of single- and double-DNA strands using graphene liquid cell TEM. For example, to improve imaging contrast, Chen *et al.* prepared single- and double-stranded DNA structures capped at one or more ends with small, ~5 nm gold nanoparticles and imaged them using moderate electron dose rates (60–100 e$^-$ Å^{-2} s^{-1}).[74] These structures exhibited ample translational and rotational diffusion in the graphene liquid pockets, which allowed the gold nanoparticle tags to be tracked for nearly 100 s (Fig. 11a and b). The highly correlated translational motion of gold nanoparticles joined by varying lengths of double-stranded DNA provided compelling evidence that phosphodiester bonds remained intact throughout the imaging process (Fig. 11c). The integrity of DNA under these imaging conditions was further verified with gold–DNA trimers, for which there was diffusional correlation for both the directly and indirectly linked gold nanoparticles (Fig. 11d–f).

More recently, Wang *et al.* used a combination of modified graphene liquid cells, radiolysis-resistant D$_2$O as a solvent, and low voltage conditions to study unlabelled DNA.[95] Liquid pockets were prepared with initially unhybridized DNA oligomers, whose diffusion, interactions, and assembly were then tracked across periods of ~100 s at dose rates of 2–10 e$^-$ Å^{-2} s^{-1}. A variety of processes were monitored. For example, in a solution of complementary oligomers, pairs of initially round, globular structures were observed to diffuse together and slowly "stretch" into a rod-like shape (Fig. 11g). This behavior was attributed to unpaired DNA strands (which are flexible, with a persistence length of ~2 nm, and therefore globular) colliding and gradually interlacing into a double-stranded DNA double helix (which is stiff, with a persistence length of ~50 nm, and therefore rod-like). A diversity of other behaviours was observed. For example, in the case of three oligomers colliding (Fig. 11h), it was observed that all would initially overlap with each other until one (represented in blue, Fig. 11h) eventually diffused away, allowing the remaining
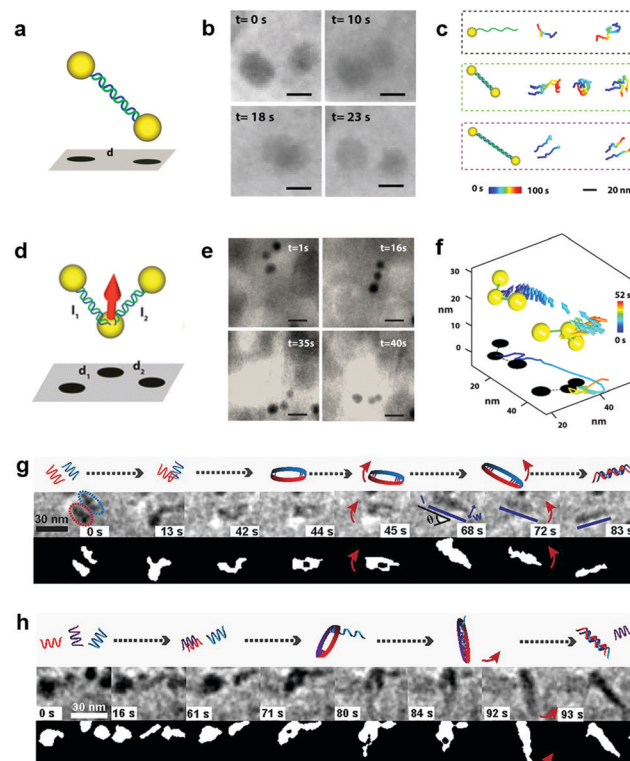

Fig. 11 Liquid phase electron microscopy of labelled (a–f) and unlabelled (g and h) DNA in graphene liquid cells. (a) Schematic and (b) representative TEM snapshots of a linear DNA strand capped with two gold nanoparticles. Rotational diffusion leads to changes in the projected view over time. (c) Example trajectories from singly-tagged DNA and doubly-tagged DNA of different lengths. (d–f) Schematic, snapshots, and tracked trajectories of a branched trimer, for which a distinct orientation can be defined. Reproduced with permission from ref. 73. Copyright 2013 American Chemical Society. (g) Trajectory of two, initially flexible and globular "halves" of a 30-basepair helix as they meet and elongate into a rod-like form. (h) "Trial-and-error" interaction when three 30-basepair sequences with different affinity meet. Reproduced from ref. 90. Copyright 2020 National Academy of Sciences.

two oligomers to "stretch" and form a hybridized rod. These and other trial-and-error events were proposed to be important for understanding transient error and error correction along pathways to DNA hybridization.

4. Outlook and conclusion

As an imaging technique with a singular combination of spatial and temporal resolution, liquid-phase electron microscopy offers a unique lens into nanoscale phenomena. The diverse ways this capability has thus far been applied in "living" systems have been highlighted in this review. Nevertheless, these efforts likely mark only the beginning of liquid-phase electron microscopy's usefulness to study biological and bio-molecular systems; through further technical and instrumental advancements, improved understanding of environments exposed to electron illumination, greater synergy with existing experimental tools, *etc.*, the capability of liquid-phase electron microscopy to

reveal exciting and meaningful biological insight are expected to greatly expand.

One route forward involves expanding the types of experiments which can be performed in liquid cells, particularly in graphene liquid cells, and especially developing protocols to do these experiments with high reproducibility. For example, with commercially available silicon nitride liquid chambers, it is already possible to apply a variety of external stimuli, such as heating/cooling, electric fields, optical (laser) stimulation, and the influx of certain solutes, and follow the subsequent evolution of the specimen in a controlled way. These capabilities have been used to monitor many processes in inorganic materials, including galvanic replacement,[71,158] charge–discharge cycles in battery materials,[159–161] drying-induced phenomena,[162] and nanoparticle assembly.[63] However, when it comes to graphene liquid cells, in which biological materials can be studied with higher contrast, higher resolution, and greater stability, such environmental control is more difficult. In particular, because graphene liquid cell "pockets" in their current form tend to be irregular in size and wholly cut off from other solutions, it is challenging to alter the encapsulated environment *in situ* without using the electron beam itself (*i.e.*, through radiolysis effects, to increase the pH or introduce radicals[90,91]). A "graphene flow cell," therefore, or a graphene liquid cell in which *in situ* mixing could be performed, would greatly expand experimental possibilities: observing how enzymes respond to the influx of their substrate, studies of biomineralization, visualizing how biomolecular fluctuations change in response to different physicochemical environments in general, *etc.* Two types of recently demonstrated, lithographically patterned graphene liquid cells[111,163] may inspire design strategies to this end. Developing more advanced liquid cell designs may also help address difficulties like controlling liquid thickness, a technical challenge currently shared by both graphene and silicon nitride liquid cells. While graphene liquid cells are irregular in size due to the stochastic formation of liquid pockets during the sealing process, in silicon nitride liquid cells it is difficult to control the liquid thickness because the thin windows of the chamber are prone to bowing outward, which is in turn sensitive to factors like the rate of liquid flow. These factors can lead to loss of reproducibility not only in sample geometry, but also (for reasons described in Section 2) resolution. One can measure the thickness of a liquid cell *in situ*, using a technique like EELS,[164] and potentially adapt the experiment accordingly, but the thickness itself is hard to control. Addressing the challenges associated with handling graphene described in Section 2 will be another important part of these efforts.

In addition to experimental capabilities, developments in data handling and image processing would offer new opportunities, particularly for very-low dose imaging. Machine learning-based strategies, for example, are becoming more and more standard in high resolution fluorescence microscopy investigations, to improve signal-to-noise, perform image segmentation, classify or identify features of interest, and in general increase the amount of useful information which can be garnered from imaging datasets.[165–168] Many of the associated algorithms are open-source or publically available. However, the

emergence of these computational approaches into liquid-phase electron microscopy investigations has been slower. Strategies like compressive sensing have begun to be applied to interrogate certain inorganic materials with liquid-phase STEM and low electron doses and/or high acquisition speeds.[169,170] In addition, we recently demonstrated a machine-learning based approach based on electron scattering theory, to segment low-dose liquid-phase electron microscopy movies and extract quantitative physical insight.[65] Nevertheless, widespread use of these types of computational tools is forthcoming. Note that machine learning-based tools may serve in many roles besides improving image quality and information content, such as to identify unique dynamic phenomena, reducing the dimensionality of complex physical datasets, *etc.*[171,172] Overall, liquid-phase electron microscopy may benefit from more widespread adoption of these and related computational tools.

Expanding correlative characterization and correlative imaging will also be an important part of making liquid-phase electron microscopy observations translatable to "real" bulk systems. So far, correlative characterization has mostly been applied in the form of correlative light–electron microscopy (CLEM), especially on studies of whole cells. In CLEM, electron microscopy primarily provides structural information, while light (fluorescence) microscopy provides primarily contextual information (*e.g.*, the presence of a specific, fluorescently labelled protein, the location of particular cellular features, *etc.*). This method is seeing increasing use in cryo-EM studies of whole cells,[173,174] where integrated microscopes are beginning to be developed, and also been applied in some liquid-phase electron microscopy studies.[109,118] However, liquid-phase electron microscopy could be partnered with a much wider variety of conventional experimental techniques, such as spectroscopic characterization, small-angle X-ray scattering, and other imaging modalities, both for fundamental studies (understanding the role of electron illumination, for instance[92,145]) and developing more "real-world" applications. Specialized liquid holders compatible with both an electron microscope and another instrument (such as an X-ray beam line) are actively being developed,[175,176] and may assist in such studies. With regard to X-ray techniques in particular, besides just scattering methods, X-ray imaging techniques can achieve ∼50 nm resolution and help provide information about elemental composition, intermediate range order, and other spectroscopic information salient to biological materials,[177] particularly cells.[178,179] These modalities may thereby serve as useful bridges between optical and electron microscopy characterization. There may also be meaningful ways to combine liquid-phase electron microscopy imaging with other electron microscopy modalities, *e.g.*, liquid-phase electron diffraction and spectroscopy, to provide crystallographic and compositional information. It must be noted, however, that the latter two tend to require much higher electron doses to achieve appreciable signal-to-noise, and so damage mitigation strategies will become particularly important.

In short, liquid-phase electron microscopy is poised to become a valuable new experimental tool for biological and biophysical investigations at many length scales. Indeed, in just ten years, the field of biological liquid-phase electron

microscopy has advanced from observing whole cells, to individual DNA strands in their native liquid environment, and technical, analytical, and theoretical advancements in the years to come are expected to push these capabilities even further. With fundamental understanding of the liquid cell environment will come the potential for new and translatable biological insight at the nanometer to atomic scale.

Conflicts of interest

There are no conflicts to declare.

Acknowledgements

References

1 Y. M. Bar-On, R. Phillips and R. Milo, *Proc. Natl. Acad. Sci. U. S. A.*, 2018, **115**, 6506–6511.

2 M. G. Burgess and S. D. Gaines, *Proc. Natl. Acad. Sci. U. S. A.*, 2018, **115**, 6328–6330.

3 W. Swartz, E. Sala, S. Tracey, R. Watson and D. Pauly, *PLoS One*, 2010, **5**, e15143.

4 D. A. Kroodsma, J. Mayorga, T. Hochberg, N. A. Miller, K. Boerder, F. Ferretti, A. Wilson, B. Bergman, T. D. White, B. A. Block, P. Woods, B. Sullivan, C. Costello and B. Worm, *Science*, 2018, **359**, 904–908.

5 M. N. Sawka, S. J. Montain and W. A. Latzka, *Comp. Biochem. Physiol., Part A: Mol. Integr. Physiol.*, 2001, **128**, 679–690.

6 C. Stöllberger, in *Comparative Medicine: Anatomy and Physiology*, ed. E. Jensen-Jarolim, Springer, Vienna, 2014, pp. 61–70.

7 J. E. Greenleaf and M. H. Harrison, *Nutrition and Aerobic Exercise*, American Chemical Society, 1986, vol. 294, pp. 107–124.

8 D. Zhong, S. K. Pal and A. H. Zewail, *Chem. Phys. Lett.*, 2011, **503**, 1–11.

9 D. S. Goodsell, in *The Machinery of Life*, ed. D. S. Goodsell, Springer, New York, NY, 2009, pp. 8–26.

10 J. Cavanagh, W. J. Fairbrother, A. G. Palmer III and N. J. Skelton, *Protein NMR Spectroscopy: Principles and Practice*, Elsevier, 1995.

11 I. R. Kleckner and M. P. Foster, *Biochim. Biophys. Acta, Proteins Proteomics*, 2011, **1814**, 942–968.

12 M. D. Tuttle, G. Comellas, A. J. Nieuwkoop, D. J. Covell, D. A. Berthold, K. D. Kloepper, J. M. Courtney, J. K. Kim, A. M. Barclay, A. Kendall, W. Wan, G. Stubbs, C. D. Schwieters, V. M. Y. Lee, J. M. George and C. M. Rienstra, *Nat. Struct. Mol. Biol.*, 2016, **23**, 409–415.

13 J. Drenth, *Principles of Protein X-Ray Crystallography*, Springer Science & Business Media, 2007.

14 E. F. Garman, *Science*, 2014, **343**, 1102–1108.

15 E. Aronoff-Spencer, C. S. Burns, N. I. Avdievich, G. J. Gerfen, J. Peisach, W. E. Antholine, H. L. Ball, F. E. Cohen, S. B. Prusiner and G. L. Millhauser, *Biochemistry*, 2000, **39**, 13760–13771.

16 H. S. Mchaourab, P. R. Steed and K. Kazmier, *Structure*, 2011, **19**, 1549–1561.

17 L. P. DeFlores, Z. Ganim, R. A. Nicodemus and A. Tokmakoff, *J. Am. Chem. Soc.*, 2009, **131**, 3385–3391.

18 Y. S. Kim and R. M. Hochstrasser, *J. Phys. Chem. B*, 2009, **113**, 8231–8251.

19 H. S. Chung, Z. Ganim, K. C. Jones and A. Tokmakoff, *Proc. Natl. Acad. Sci. U. S. A.*, 2007, **104**, 14237–14242.

20 H. Frauenfelder, S. G. Sligar and P. G. Wolynes, *Science*, 1991, **254**, 1598–1603.

21 Y. Shi, *Cell*, 2014, **159**, 995–1014.

22 L. Barbieri, E. Luchinat and L. Banci, *Sci. Rep.*, 2015, **5**, 1–9.

23 P. Rajagopal, E. B. Waygood, J. Reizer, M. H. Saier and R. E. Klevit, *Protein Sci.*, 1997, **6**, 2624–2627.

24 C. J. Mann, L. Yu, C.-M. Lo and M. K. Kim, *Opt. Express*, 2005, **13**, 8693–8698.

25 Y. Park, C. A. Best, K. Badizadegan, R. R. Dasari, M. S. Feld, T. Kuriabova, M. L. Henle, A. J. Levine and G. Popescu, *Proc. Natl. Acad. Sci. U. S. A.*, 2010, **107**, 6731–6736.

26 M. Muller, *Introduction to Confocal Fluorescence Microscopy*, SPIE Press, 2006.

27 S. Nie, D. T. Chiu and R. N. Zare, *Science*, 1994, **266**, 1018–1021.

28 K. N. Fish, *Curr. Protoc. Cytom.*, 2009, **50**, 12.18.1–12.18.13.

29 S. W. Hell and J. Wichmann, *Opt. Lett.*, 1994, **19**, 780–782.

30 B. Hein, K. I. Willig and S. W. Hell, *Proc. Natl. Acad. Sci. U. S. A.*, 2008, **105**, 14271–14276.

31 E. Betzig, G. H. Patterson, R. Sougrat, O. W. Lindwasser, S. Olenych, J. S. Bonifacino, M. W. Davidson, J. Lippincott-Schwartz and H. F. Hess, *Science*, 2006, **313**, 1642–1645.

32 S. Manley, J. M. Gillette, G. H. Patterson, H. Shroff, H. F. Hess, E. Betzig and J. Lippincott-Schwartz, *Nat. Methods*, 2008, **5**, 155–157.

33 H. Shroff, C. G. Galbraith, J. A. Galbraith and E. Betzig, *Nat. Methods*, 2008, **5**, 417–423.

34 M. J. Rust, M. Bates and X. Zhuang, *Nat. Methods*, 2006, **3**, 793–795.

35 F. Balzarotti, Y. Eilers, K. C. Gwosch, A. H. Gynnå, V. Westphal, F. D. Stefani, J. Elf and S. W. Hell, *Science*, 2017, **355**, 606–612.

36 K. C. Gwosch, J. K. Pape, F. Balzarotti, P. Hoess, J. Ellenberg, J. Ries and S. W. Hell, *Nat. Methods*, 2020, **17**, 217–224.

37 A. Yildiz, J. N. Forkey, S. A. McKinney, T. Ha, Y. E. Goldman and P. R. Selvin, *Science*, 2003, **300**, 2061–2065.

38 A. Yildiz, M. Tomishige, R. D. Vale and P. R. Selvin, *Science*, 2004, **303**, 676–678.

39 D. A. Muller, L. F. Kourkoutis, M. Murfitt, J. H. Song, H. Y. Hwang, J. Silcox, N. Dellby and O. L. Krivanek, *Science*, 2008, **319**, 1073–1076.

40 A. M. van der Zande, P. Y. Huang, D. A. Chenet, T. C. Berkelbach, Y. You, G.-H. Lee, T. F. Heinz, D. R. Reichman, D. A. Muller and J. C. Hone, *Nat. Mater.*, 2013, **12**, 554–561.

41 R. Fernandez-Leiro and S. H. W. Scheres, *Nature*, 2016, **537**, 339–346.

42 M. P. M. H. Benoit, A. B. Asenjo and H. Sosa, *Nat. Commun.*, 2018, **9**, 1–13.

43 X. Zhang, E. Settembre, C. Xu, P. R. Dormitzer, R. Bellamy, S. C. Harrison and N. Grigorieff, *Proc. Natl. Acad. Sci. U. S. A.*, 2008, **105**, 1867–1872.

44 D. F. Parsons, *Science*, 1974, **186**, 407–414.

45 J. W. Smith, X. Jiang, H. An, A. M. Barclay, G. Licari, E. Tajkhorshid, E. G. Moore, C. M. Rienstra, J. S. Moore and Q. Chen, *ACS Appl. Nano Mater.*, 2020, **3**, 937–945.

46 S. De Carlo and J. R. Harris, *Micron*, 2011, **42**, 117–131.

47 J. N. Skepper and J. M. Powell, *Cold Spring Harb. Protoc.*, 2008, DOI: 10.1101/pdb.prot5015.

48 F. A. Pacheco, I. Pinnau, M. Reinhard and J. O. Leckie, *J. Membr. Sci.*, 2010, **358**, 51–59.

49 D. F. Parsons, V. R. Matricardi, R. C. Moretz and J. N. Turner, in *Advances in Biological and Medical Physics*, ed. J. H. Lawrence and J. W. Gofman, Elsevier, 1974, vol. 15, pp. 161–270.

50 D. L. Dorset and D. F. Parsons, *Acta Crystallogr., Sect. A: Cryst. Phys., Diffr., Theor. Gen. Crystallogr.*, 1975, **31**, 210–215.

51 I. M. Abrams and J. W. McBain, *J. Appl. Phys.*, 1944, **15**, 607–609.

52 E. Ruska, *Kolloid-Z.*, 1942, **100**, 212–219.

53 J. Frank, *J. Struct. Biol.*, 2017, **200**, 303–306.

54 S. Kaledhonkar, Z. Fu, H. White and J. Frank, *Methods Mol. Biol.*, 2018, **1764**, 59–71.

55 J. Frank and A. Ourmazd, *Methods*, 2016, **100**, 61–67.

56 E. A. Ring and N. de Jonge, *Microsc. Microanal.*, 2010, **16**, 622–629.

57 M. P. Rossi, H. Ye, Y. Gogotsi, S. Babu, P. Ndungu and J.-C. Bradley, *Nano Lett.*, 2004, **4**, 989–993.

58 A. Kolmakov, D. A. Dikin, L. J. Cote, J. Huang, M. K. Abyaneh, M. Amati, L. Gregoratti, S. Günther and M. Kiskinova, *Nat. Nanotechnol.*, 2011, **6**, 651–657.

59 J. M. Yuk, J. Park, P. Ercius, K. Kim, D. J. Hellebusch, M. F. Crommie, J. Y. Lee, A. Zettl and A. P. Alivisatos, *Science*, 2012, **336**, 61–64.

60 N. de Jonge and F. M. Ross, *Nat. Nanotechnol.*, 2011, **6**, 695–704.

61 F. M. Ross, *Science*, 2015, **350**, aaa9886.

62 J. Kim, Z. Ou, M. R. Jones, X. Song and Q. Chen, *Nat. Commun.*, 2017, **8**, 761.

63 B. Luo, J. W. Smith, Z. Ou and Q. Chen, *Acc. Chem. Res.*, 2017, **50**, 1125–1133.

64 Z. Ou, Z. Wang, B. Luo, E. Luijten and Q. Chen, *Nat. Mater.*, 2020, **19**, 450–455.

65 L. Yao, Z. Ou, B. Luo, C. Xu and Q. Chen, *ACS Cent. Sci.*, DOI: 10.1021/acscentsci.0c00430.

66 H.-G. Liao, D. Zherebetskyy, H. Xin, C. Czarnik, P. Ercius, H. Elmlund, M. Pan, L.-W. Wang and H. Zheng, *Science*, 2014, **345**, 916–919.

67 X. Ye, M. R. Jones, L. B. Frechette, Q. Chen, A. S. Powers, P. Ercius, G. Dunn, G. M. Rotskoff, S. C. Nguyen, V. P. Adiga, A. Zettl, E. Rabani, P. L. Geissler and A. P. Alivisatos, *Science*, 2016, **354**, 874–877.

68 M. J. Williamson, R. M. Tromp, P. M. Vereecken, R. Hull and F. M. Ross, *Nat. Mater.*, 2003, **2**, 532–536.

69 N. M. Schneider, M. M. Norton, B. J. Mendel, J. M. Grogan, F. M. Ross and H. H. Bau, *J. Phys. Chem. C*, 2014, **118**, 22373–22382.

70 J. M. Grogan, N. M. Schneider, F. M. Ross and H. H. Bau, *Nano Lett.*, 2014, **14**, 359–364.

71 S. W. Chee, S. F. Tan, Z. Baraissov, M. Bosman and U. Mirsaidov, *Nat. Commun.*, 2017, **8**, 1–8.

72 E. R. White, M. Mecklenburg, S. B. Singer, S. Aloni and B. C. Regan, *Appl. Phys. Express*, 2011, **4**, 055201.

73 U. M. Mirsaidov, H. Zheng, D. Bhattacharya, Y. Casana and P. Matsudaira, *Proc. Natl. Acad. Sci. U. S. A.*, 2012, **109**, 7187–7190.

74 Q. Chen, J. M. Smith, J. Park, K. Kim, D. Ho, H. I. Rasool, A. Zettl and A. P. Alivisatos, *Nano Lett.*, 2013, **13**, 4556–4561.

75 S. W. Chee, Z. Baraissov, N. D. Loh, P. T. Matsudaira and U. Mirsaidov, *J. Phys. Chem. C*, 2016, **120**, 20462–20470.

76 K. H. Nagamanasa, H. Wang and S. Granick, *Adv. Mater.*, 2017, **29**, 1703555.

77 M. T. Proetto, A. M. Rush, M.-P. Chien, P. Abellan Baeza, J. P. Patterson, M. P. Thompson, N. H. Olson, C. E. Moore, A. L. Rheingold, C. Andolina, J. Millstone, S. B. Howell, N. D. Browning, J. E. Evans and N. C. Gianneschi, *J. Am. Chem. Soc.*, 2014, **136**, 1162–1165.

78 A. Ianiro, H. Wu, M. M. J. van Rijt, M. P. Vena, A. D. A. Keizer, A. C. C. Esteves, R. Tuinier, H. Friedrich, N. A. J. M. Sommerdijk and J. P. Patterson, *Nat. Chem.*, 2019, **11**, 320–328.

79 N. de Jonge, *J. Microsc.*, 2018, **269**, 134–142.

80 N. de Jonge, L. Houben, R. E. Dunin-Borkowski and F. M. Ross, *Nat. Rev. Mater.*, 2019, **4**, 61–78.

81 S. M. Rehn and M. R. Jones, *ACS Energy Lett.*, 2018, **3**, 1269–1278.

82 H.-G. Liao and H. Zheng, *Annu. Rev. Phys. Chem.*, 2016, **67**, 719–747.

83 H. Wu, H. Friedrich, J. P. Patterson, N. A. J. M. Sommerdijk and N. de Jonge, *Adv. Mater.*, 2020, **32**, 2001582.

84 J. Hattne, D. Shi, C. Glynn, C.-T. Zee, M. Gallagher-Jones, M. W. Martynowycz, J. A. Rodriguez and T. Gonen, *Structure*, 2018, **26**, 759–766.

85 R. M. Glaeser, *J. Ultrastruct. Res.*, 1971, **36**, 466–482.

86 S. B. Hayward and R. M. Glaeser, *Ultramicroscopy*, 1979, **4**, 201–210.

87 R. F. Egerton, *Microsc. Res. Tech.*, 2012, **75**, 1550–1556.

88 R. F. Egerton, P. Li and M. Malac, *Micron*, 2004, **35**, 399–409.

89 T. Gupta, N. M. Schneider, J. H. Park, D. Steingart and F. M. Ross, *Nanoscale*, 2018, **10**, 7702–7710.

90 M. R. Hauwiller, J. C. Ondry, C. M. Chan, P. Khandekar, J. Yu and A. P. Alivisatos, *J. Am. Chem. Soc.*, 2019, **141**, 4428–4437.

91 M. R. Hauwiller, L. B. Frechette, M. R. Jones, J. C. Ondry, G. M. Rotskoff, P. Geissler and A. P. Alivisatos, *Nano Lett.*, 2018, **18**, 5731–5737.

92 J. Kim, M. R. Jones, Z. Ou and Q. Chen, *ACS Nano*, 2016, **10**, 9801–9808.

93 T. J. Woehl and P. Abellan, *J. Microsc.*, 2017, **265**, 135–147.
94 H. Wang, K. H. Nagamanasa, Y.-J. Kim, O.-H. Kwon and S. Granick, *ACS Nano*, 2018, **12**, 8572–8578.
95 H. Wang, B. Li, Y.-J. Kim, O.-H. Kwon and S. Granick, *Proc. Natl. Acad. Sci. U. S. A.*, 2020, **117**, 1283–1292.
96 E. Hayon, *J. Phys. Chem.*, 1965, **69**, 2628–2632.
97 P. Cioni and G. B. Strambini, *Biophys. J.*, 2002, **82**, 3246–3253.
98 Y. M. Efimova, S. Haemers, B. Wierczinski, W. Norde and A. A. van Well, *Biopolymers*, 2007, **85**, 264–273.
99 W. Bild, V. Năstasă and I. Haulică, *Rom. J. Physiol.*, 2004, **41**, 53–67.
100 A. Olgun, *Theor. Biol. Med. Modell.*, 2007, **4**, 9.
101 M. Farnum and C. Zukoski, *Biophys. J.*, 1999, **76**, 2716–2726.
102 V. Vagenende, M. G. S. Yap and B. L. Trout, *Biochemistry*, 2009, **48**, 11084–11096.
103 N. de Jonge, *Ultramicroscopy*, 2018, **187**, 113–125.
104 N. de Jonge, D. B. Peckys, G. J. Kremers and D. W. Piston, *Proc. Natl. Acad. Sci. U. S. A.*, 2009, **106**, 2159–2164.
105 N. de Jonge, N. Poirier-Demers, H. Demers, D. B. Peckys and D. Drouin, *Ultramicroscopy*, 2010, **110**, 1114–1119.
106 C. J. Russo and L. A. Passmore, *Curr. Opin. Struct. Biol.*, 2016, **37**, 81–89.
107 C. J. Russo and L. A. Passmore, *Nat. Methods*, 2014, **11**, 649–652.
108 H. Cho, M. R. Jones, S. C. Nguyen, M. R. Hauwiller, A. Zettl and A. P. Alivisatos, *Nano Lett.*, 2017, **17**, 414–420.
109 J. Park, H. Park, P. Ercius, A. F. Pegoraro, C. Xu, J. W. Kim, S. H. Han and D. A. Weitz, *Nano Lett.*, 2015, **15**, 4737–4744.
110 K. Naydenova, M. J. Peet and C. J. Russo, *Proc. Natl. Acad. Sci. U. S. A.*, 2019, **116**, 11718–11724.
111 D. J. Kelly, M. Zhou, N. Clark, M. J. Hamer, E. A. Lewis, A. M. Rakowski, S. J. Haigh and R. V. Gorbachev, *Nano Lett.*, 2018, **18**, 1168–1174.
112 P. M. G. van Deursen, R. I. Koning, V. Tudor, M.-A. Moradi, J. P. Patterson, A. Kros, N. A. J. M. Sommerdijk, A. J. Koster and G. F. Schneider, *Adv. Funct. Mater.*, 2020, **30**, 1904468.
113 M. Textor and N. de Jonge, *Nano Lett.*, 2018, **18**, 3313–3321.
114 Y. Sasaki, R. Kitaura, J. M. Yuk, A. Zettl and H. Shinohara, *Chem. Phys. Lett.*, 2016, **650**, 107–112.
115 S. Keskin and N. de Jonge, *Nano Lett.*, 2018, **18**, 7435–7440.
116 M. Winey, J. B. Meehl, E. T. O'Toole and T. H. Giddings, *Mol. Biol. Cell*, 2014, **25**, 319–323.
117 D. D. Sabatini, K. Bensch and R. J. Barrnett, *J. Cell Biol.*, 1963, **17**, 19–58.
118 D. B. Peckys, U. Korf and N. de Jonge, *Sci. Adv.*, 2015, **1**, e1500165.
119 E. Kennedy, E. M. Nelson, T. Tanaka, J. Damiano and G. Timp, *ACS Nano*, 2016, **10**, 2669–2677.
120 W. J. Dearnaley, B. Schleupner, A. C. Varano, N. A. Alden, F. Gonzalez, M. A. Casasanta, B. E. Scharf, M. J. Dukes and D. F. Kelly, *Nano Lett.*, 2019, **19**, 6734–6741.
121 E. S. Pohlmann, K. Patel, S. Guo, M. J. Dukes, Z. Sheng and D. F. Kelly, *Nano Lett.*, 2015, **15**, 2329–2335.
122 I. N. Dahmke, A. Verch, J. Hermannsdörfer, D. B. Peckys, R. S. Weatherup, S. Hofmann and N. de Jonge, *ACS Nano*, 2017, **11**, 11108–11117.
123 M. Wojcik, M. Hauser, W. Li, S. Moon and K. Xu, *Nat. Commun.*, 2015, **6**, 1–6.
124 S. Besztejan, S. Keskin, S. Manz, G. Kassier, R. Bücker, D. Venegas-Rojas, H. K. Trieu, A. Rentmeister and R. J. D. Miller, *Microsc. Microanal.*, 2017, **23**, 46–55.
125 D. B. Peckys, P. Mazur, K. L. Gould and N. de Jonge, *Biophys. J.*, 2011, **100**, 2522–2529.
126 N. de Jonge and D. B. Peckys, *ACS Nano*, 2016, **10**, 9061–9063.
127 R. M. Glaeser, *Biophys. J.*, 2012, **103**, 163–164.
128 M. C. Scott, C.-C. Chen, M. Mecklenburg, C. Zhu, R. Xu, P. Ercius, U. Dahmen, B. C. Regan and J. Miao, *Nature*, 2012, **483**, 444–447.
129 X. Song, J. W. Smith, J. Kim, N. J. Zaluzec, W. Chen, H. An, J. M. Dennison, D. G. Cahill, M. A. Kulzick and Q. Chen, *ACS Appl. Mater. Interfaces*, 2019, **11**, 8517–8526.
130 W. Wan and J. A. G. Briggs, in *Methods in Enzymology*, ed. R. A. Crowther, Academic Press, 2016, vol. 579, pp. 329–367.
131 K. Koo, K. S. Dae, Y. K. Hahn and J. M. Yuk, *Nano Lett.*, 2020, **20**, 4708–4713.
132 B. L. Nannenga and T. Gonen, *Nat. Methods*, 2019, **16**, 369–379.
133 S. H. Kim, M. J. Misner, T. Xu, M. Kimura and T. P. Russell, *Adv. Mater.*, 2004, **16**, 226–231.
134 Y. Diao, B. C.-K. Tee, G. Giri, J. Xu, D. H. Kim, H. A. Becerril, R. M. Stoltenberg, T. H. Lee, G. Xue, S. C. B. Mannsfeld and Z. Bao, *Nat. Mater.*, 2013, **12**, 665–671.
135 M. A. Boles, M. Engel and D. V. Talapin, *Chem. Rev.*, 2016, **116**, 11220–11289.
136 L. M. DiMemmo, A. C. Varano, J. Haulenbeek, Y. Liang, K. Patel, M. J. Dukes, S. Zheng, M. Hubert, S. P. Piccoli and D. F. Kelly, *Lab Chip*, 2017, **17**, 315–322.
137 K. D. Ratanji, J. P. Derrick, R. J. Dearman and I. Kimber, *J. Immunotoxicol.*, 2014, **11**, 99–109.
138 P. Arosio, T. P. J. Knowles and S. Linse, *Phys. Chem. Chem. Phys.*, 2015, **17**, 7606–7618.
139 Y. Liu, X. Wang and C. B. Ching, *Cryst. Growth Des.*, 2010, **10**, 548–558.
140 M. C. R. Heijna, W. J. P. van Enckevort and E. Vlieg, *Cryst. Growth Des.*, 2008, **8**, 270–274.
141 T. Yamazaki, Y. Kimura, P. G. Vekilov, E. Furukawa, M. Shirai, H. Matsumoto, A. E. S. V. Driessche and K. Tsukamoto, *Proc. Natl. Acad. Sci. U. S. A.*, 2017, **114**, 2154–2159.
142 T. Yamazaki, A. E. S. V. Driessche and Y. Kimura, *Soft Matter*, 2020, **16**, 1955–1960.
143 P. R. ten Wolde and D. Frenkel, *Science*, 1997, **277**, 1975–1978.
144 A. Sauter, F. Roosen-Runge, F. Zhang, G. Lotze, A. Feoktystov, R. M. J. Jacobs and F. Schreiber, *Faraday Discuss.*, 2015, **179**, 41–58.
145 M. A. Touve, A. S. Carlini and N. C. Gianneschi, *Nat. Commun.*, 2019, **10**, 1–12.
146 M. Feric, N. Vaidya, T. S. Harmon, D. M. Mitrea, L. Zhu, T. M. Richardson, R. W. Kriwacki, R. V. Pappu and C. P. Brangwynne, *Cell*, 2016, **165**, 1686–1697.
147 Y. Shin and C. P. Brangwynne, *Science*, 2017, **357**, eaaf4382.
148 H. Le Ferrand, M. Duchamp, B. Gabryelczyk, H. Cai and A. Miserez, *J. Am. Chem. Soc.*, 2019, **141**, 7202–7210.

149 B. L. Gilmore, S. P. Showalter, M. J. Dukes, J. R. Tanner, A. C. Demmert, S. M. McDonald and D. F. Kelly, *Lab Chip*, 2012, **13**, 216–219.

150 A. C. Varano, A. Rahimi, M. J. Dukes, S. Poelzing, S. M. McDonald and D. F. Kelly, *Chem. Commun.*, 2015, **51**, 16176–16179.

151 C. Wang, Q. Qiao, T. Shokuhfar and R. F. Klie, *Adv. Mater.*, 2014, **26**, 3410–3414.

152 U. M. Mirsaidov, H. Zheng, Y. Casana and P. Matsudaira, *Biophys. J.*, 2012, **102**, L15–L17.

153 C. Colliex, T. Manoubi and C. Ortiz, *Phys. Rev. B: Condens. Matter Mater. Phys.*, 1991, **44**, 11402–11411.

154 L. A. J. Garvie and P. R. Buseck, *Nature*, 1998, **396**, 667–670.

155 T. T. Perkins, S. R. Quake, D. E. Smith and S. Chu, *Science*, 1994, **264**, 822–826.

156 C. M. Schroeder, H. P. Babcock, E. S. G. Shaqfeh and S. Chu, *Science*, 2003, **301**, 1515–1519.

157 C. M. Schroeder, R. E. Teixeira, E. S. G. Shaqfeh and S. Chu, *Macromolecules*, 2005, **38**, 1967–1978.

158 E. A. Sutter and P. W. Sutter, *Nanoscale*, 2017, **9**, 1271–1278.

159 D. Lee, H. Park, Y. Ko, H. Park, T. Hyeon, K. Kang and J. Park, *J. Am. Chem. Soc.*, 2019, **141**, 8047–8052.

160 M. Gu, L. R. Parent, B. L. Mehdi, R. R. Unocic, M. T. McDowell, R. L. Sacci, W. Xu, J. G. Connell, P. Xu, P. Abellan, X. Chen, Y. Zhang, D. E. Perea, J. E. Evans, L. J. Lauhon, J.-G. Zhang, J. Liu, N. D. Browning, Y. Cui, I. Arslan and C.-M. Wang, *Nano Lett.*, 2013, **13**, 6106–6112.

161 T. Shang, Y. Wen, D. Xiao, L. Gu, Y.-S. Hu and H. Li, *Adv. Energy Mater.*, 2017, **7**, 1700709.

162 W. C. Lee, B. H. Kim, S. Choi, S. Takeuchi and J. Park, *J. Phys. Chem. Lett.*, 2017, **8**, 647–654.

163 K. Lim, Y. Bae, K. Kim, S. Jeon, B. H. Kim, J. Park and W. C. Lee, *2019 IEEE 32nd International Conference on Micro Electro Mechanical Systems (MEMS)*, 2019, pp. 105–106.

164 E. A. Lewis, S. J. Haigh, T. J. A. Slater, Z. He, M. A. Kulzick, M. G. Burke and N. J. Zaluzec, *Chem. Commun.*, 2014, **50**, 10019–10022.

165 T. Falk, D. Mai, R. Bensch, Ö. Çiçek, A. Abdulkadir, Y. Marrakchi, A. Böhm, J. Deubner, Z. Jäckel, K. Seiwald, A. Dovzhenko, O. Tietz, C. Dal Bosco, S. Walsh, D. Saltukoglu, T. L. Tay, M. Prinz, K. Palme, M. Simons, I. Diester, T. Brox and O. Ronneberger, *Nat. Methods*, 2019, **16**, 67–70.

166 W. Ouyang, F. Mueller, M. Hjelmare, E. Lundberg and C. Zimmer, *Nat. Methods*, 2019, **16**, 1199–1200.

167 H. Wang, Y. Rivenson, Y. Jin, Z. Wei, R. Gao, H. Günaydın, L. A. Bentolila, C. Kural and A. Ozcan, *Nat. Methods*, 2019, **16**, 103–110.

168 E. Moen, D. Bannon, T. Kudo, W. Graf, M. Covert and D. Van Valen, *Nat. Methods*, 2019, **16**, 1233–1246.

169 A. Stevens, L. Kovarik, P. Abellan, X. Yuan, L. Carin and N. D. Browning, *Adv. Struct. Chem. Imaging*, 2015, **1**, 10.

170 A. Stevens, H. Yang, L. Carin, I. Arslan and N. D. Browning, *Microscopy*, 2014, **63**, 41–51.

171 I. T. Jolliffe and J. Cadima, *Philos. Trans. R. Soc., A*, 2016, **374**, 20150202.

172 A. W. Long and A. L. Ferguson, *J. Phys. Chem. B*, 2014, **118**, 4228–4244.

173 P. de Boer, J. P. Hoogenboom and B. N. G. Giepmans, *Nat. Methods*, 2015, **12**, 503–513.

174 I. Begemann and M. Galic, *Front. Synaptic Neurosci.*, 2016, **8**, 28.

175 T. S. Arthur, P.-A. Glans, N. Singh, O. Tutusaus, K. Nie, Y.-S. Liu, F. Mizuno, J. Guo, D. H. Alsem, N. J. Salmon and R. Mohtadi, *Chem. Mater.*, 2017, **29**, 7183–7188.

176 J. Lim, Y. Li, D. H. Alsem, H. So, S. C. Lee, P. Bai, D. A. Cogswell, X. Liu, N. Jin, Y. Yu, N. J. Salmon, D. A. Shapiro, M. Z. Bazant, T. Tyliszczak and W. C. Chueh, *Science*, 2016, **353**, 566–571.

177 J. D. Brock and M. Sutton, *Mater. Today*, 2008, **11**, 52–55.

178 J. Kirz, C. Jacobsen and M. Howells, *Q. Rev. Biophys.*, 1995, **28**, 33–130.

179 V. Weinhardt, J.-H. Chen, A. Ekman, G. McDermott, M. A. Le Gros and C. Larabell, *Biochem. Soc. Trans.*, 2019, **47**, 489–508.